




The Deubiquitylase Otub1 Regulates the Chemotactic Response of Splenic B Cells by Modulating the Stability of the γ -Subunit Gng2

Vincent M. Luo^{a,b}, Connie Shen^{a,c*}, Samantha Worme^{b,d*}, Aanya Bhagrath^{c,e*}, Estelle Simo-Cheyrou^a, Steven Findlay^{b,d}, Steven Hébert^{b,f}, William Wai Lam Poon^{b,d}, Zahra Aryanpour^b, Thomas Zhang^b, René P. Zahedi^{g,h,i,j}, Jonathan Boulais^k, Zachary S. Buchwald^l, Christoph H. Borchers^{m,n,o}, Jean-Francois Côté^{k,p,q,r}, Claudia L. Kleinman^{b,f}, Judith N. Mandl^{a,c,e} and Alexandre Orthwein^{a,b,d,l,n} 

^aDepartment of Microbiology and Immunology, McGill University, Montréal, Québec, Canada; ^bLady Davis Institute for Medical Research, Jewish General Hospital, Montréal, Québec, Canada; ^cMcGill Research Centre for Complex Traits, McGill University, Montréal, Québec, Canada; ^dDivision of Experimental Medicine, McGill University, Montréal, Québec, Canada; ^eDepartment of Physiology, McGill University, Montréal, Québec, Canada; ^fDepartment of Human Genetics, McGill University, Montréal, Québec, Canada; ^gManitoba Centre for Proteomics & Systems Biology, University of Manitoba, Winnipeg, Manitoba, Canada; ^hDepartment of Internal Medicine, University of Manitoba, Winnipeg, Manitoba, Canada; ⁱDepartment of Biochemistry and Medical Genetics, University of Manitoba, Winnipeg, Manitoba, Canada; ^jCancerCare Manitoba Research Institute, Winnipeg, Manitoba, Canada; ^kInstitut de Recherches Cliniques de Montréal (IRCM), Montreal, Québec, Canada; ^lDepartment of Radiation Oncology, Winship Cancer Institute, Emory University, Atlanta, Georgia, USA; ^mSegal Cancer Proteomics Centre, Lady Davis Institute for Medical Research, McGill University, Montréal, Québec, Canada; ⁿGerald Bronfman Department of Oncology, Lady Davis Institute for Medical Research, Jewish General Hospital, Montréal, Québec, Canada; ^oDepartment of Pathology, McGill University, Montreal, Québec, Canada; ^pDepartment of Anatomy and Cell Biology, McGill University, Montreal, Québec, Canada; ^qDépartement de Biochimie et Médecine Moléculaire, Université de Montréal, Montreal, Québec, Canada; ^rDépartement de Médecine (Programmes de Biologie Moléculaire), Université de Montréal, Montreal, Québec, Canada

ABSTRACT

The ubiquitin proteasome system performs the covalent attachment of lysine 48-linked polyubiquitin chains to substrate proteins, thereby targeting them for degradation, while deubiquitylating enzymes (DUBs) reverse this process. This posttranslational modification regulates key features both of innate and adaptive immunity, including antigen presentation, protein homeostasis and signal transduction. Here we show that loss of one of the most highly expressed DUBs, Otub1, results in changes in murine splenic B cell subsets, leading to a significant increase in marginal zone and transitional B cells and a concomitant decrease in follicular B cells. We demonstrate that Otub1 interacts with the γ -subunit of the heterotrimeric G protein, Gng2, and modulates its ubiquitylation status, thereby controlling Gng2 stability. Proximal mapping of Gng2 revealed an enrichment in partners associated with chemokine signaling, actin cytoskeleton and cell migration. In line with these findings, we show that *Otub1*-deficient B cells exhibit greater Ca^{2+} mobilization, F-actin polymerization and chemotactic responsiveness to Cxcl12, Cxcl13 and S1P *in vitro*, which manifests *in vivo* as altered localization of B cells within the spleen. Together, our data establishes Otub1 as a novel regulator of G-protein coupled receptor signaling in B cells, regulating their differentiation and positioning in the spleen.

ARTICLE HISTORY

Received 15 March 2023
Revised 4 November 2023
Accepted 28 November 2023

KEYWORDS

Deubiquitylase, chemotaxis, deubiquitylation, B cell, heterotrimeric G protein gamma subunit 2 (γ -subunit), spleen, marginal zone, chemokine receptor

Introduction

The covalent attachment of one or multiple ubiquitin (Ub) molecules onto proteins, termed ubiquitylation, has emerged as an important regulatory pathway in both innate and adaptive immune cells.¹ Ubiquitylation is a multistep process which is initiated by an E1 Ub activating enzyme, followed by an E2 Ub conjugating enzyme, and an E3 Ub ligase that collaborates with the E2 to mediate the transfer of Ub to a lysine or an N-terminal methionine residue on the target protein.² Critically, ubiquitylation is a reversible process where Ub moieties can be removed from substrates via ubiquitin-specific proteases, named deubiquitylating enzymes (DUBs).³

One of the most highly expressed DUBs in humans and mice is OTUB1,⁴ which preferentially cleaves lysine-48 (K48)-linked polyUb chains through its catalytic triad residues D88/C91/H265.^{5,6} K48-linked polyUb chains are the most abundant and the canonical signal for protein degradation via the 26S proteasome, a process that actively reduces the stability of a protein.^{7,8} OTUB1 has been implicated in the cleavage of K48-linked polyUb chains on several substrates, including GRAIL,⁹ phosphorylated SMAD2/3,¹⁰ and NF- κ B/p100,¹¹ thereby promoting their stability and modulating key cellular processes such as IL-2, TGF- β or NF- κ B signaling, respectively. In addition to its deubiquitylating activity, OTUB1 has the unique ability to inhibit ubiquitin transfer in a manner that

CONTACT Alexandre Orthwein  alexandre.orthwein@emory.edu

*Contributed equally.

 Supplemental data for this article can be accessed online at [10.1080/10985549.2023.2290434](https://doi.org/10.1080/10985549.2023.2290434).

© 2024 Taylor & Francis Group, LLC

does not depend upon its catalytic activity by sequestering the E2 conjugating enzyme UBC13, thereby preventing its association to the E3 Ub ligase RNF168.¹² This process is central in mitigating the lysine-63 (K63)-linked Ub-dependent signaling of DNA double-strand breaks by controlling the transfer of Ub onto histones.^{12,13} Given the reliance of B cells on: (i) IL-2, TGF- β and NF- κ B signaling pathways for their development;^{14,15} and (ii) DNA repair processes to express a functional B cell receptor (BCR),¹⁶ we therefore hypothesized that Otub1 may play a role in B cell development.

The development and maturation of B cells is a tightly regulated process involving a series of differentiation steps in the bone marrow (BM), after which B cells enter the peripheral circulation and populate secondary lymphoid organs, the spleen and lymph nodes.¹⁷ Transitional B (TrB) cells in the spleen can develop into one of two mature B lymphocyte lineages: follicular B (FoB) cells or marginal zone B (MZB) cells. FoB and MZB cells differ both in their function as well as in their anatomical location within the spleen.¹⁸ FoB cells circulate between blood and secondary lymphoid organs, locating in areas adjacent to the T cell zone within B cell follicles in the splenic white pulp and subcapsular regions of the lymph node.¹⁹ This spatial distribution enables them to obtain the T-dependent signals on which they rely to respond to antigens. In contrast, MZB cells are resident cells of the spleen and are located at the interface between the red and white pulp. The unique positioning of MZB cells exposes them to slow-flowing blood, and poises them to respond rapidly to blood-borne pathogens.²⁰ Interestingly, defects in BCR signaling and germinal center reaction have been attributed to the UPS, in part due to the rapid turnover of CD79A, IRF4, and AID which all play key roles in shaping the B cell response.^{21–23}

Here, we generated a B cell specific *Otub1* knockout mouse and observed that Otub1 deficiency shifts the balance between TrB, FoB and MZB cells within the spleen, marked by a \sim 3-fold increase in the number of MZB cells. We determined that Otub1 modulates the stability and polyubiquitination status of the γ -subunit of the heterotrimeric G protein Gng2. In line with these findings, we showed that Otub1-depleted murine B cells are hyperresponsive to the homeostatic chemokines Cxcl12, Cxcl13 and S1P *in vitro*, all of which are known to determine mature B cell positioning within the spleen.²⁴ Strikingly, the loss of Otub1 altered the positioning of splenic B cells *in vivo*. Altogether, our data uncover a novel role for the deubiquitylase Otub1 in regulating GPCR signaling in B cells, thereby controlling their localization within the spleen.

Results

Loss of Otub1 DUB activity leads to changes in mature splenic B cell subset representation

Otub1 is a 31 kDa protein which contains a canonical catalytic triad (D88/C91/H265), an E2 binding site (T134 residue) and two Ub binding sites (Figure 1A). Previous work demonstrated that constitutive deletion of Otub1 resulted in late embryonic lethality in mice.²⁵ We therefore used the *Cd79a/Mb1-Cre*

mouse strain,²⁶ and crossed these mice with engineered mice where the *Otub1* allele was flanked with *loxP* sites (*Otub1^{fl/fl}*; control) to generate B cell-specific *Otub1* conditional knockouts, *Mb1^{Cre/+}.Otub1^{fl/fl}* (B-Otub1-fl/fl) (Figure 1B). We confirmed that Otub1 mRNA and protein expression was significantly reduced in B-Otub1-fl/fl B220⁺ B cells compared to Cre-negative controls. Importantly, Otub1 expression remained unchanged in B220⁻ cells, thereby confirming the B cell specificity of the Cre-mediated deletion (Supplementary material, Figure S1A and B).

We focused our initial analysis on the impact of Otub1 deficiency on B cell development in the bone marrow (BM). We delineated six different stages of B cell development in the BM, named the Hardy fractions (A to F),²⁷ based on the cell surface expression of B220, CD43, BP-1, CD24, IgD and IgM. This flow cytometry-based analysis showed normal percentages and numbers of pro-, pre- and immature B cells (fractions A-E) (Supplementary material, Figure S1C and D). However, we noticed a significant decrease in the percentage of recirculating mature B cells (F fraction, B220⁺CD43⁻IgM⁺IgD⁺; Supplementary material, Figure S1D), suggesting a possible role for Otub1 in B cell maturation outside the BM.

These data prompted us to further investigate the impact of Otub1 deletion on B cell maturation in the periphery. Interestingly, we observed a 5-fold increase in the percentage of MZB cells in the spleen, which translated into a \sim 3-fold increase in the total number of MZB cells within the spleen (Figure 1C and D). TrB cells (B220⁺, CD21⁻, CD23⁻) were also enriched in B-Otub1-fl/fl mice, albeit to a lesser extent (\sim 2-fold, Figure 1C and D). Importantly, these changes were accompanied by a decrease of \sim 20% in both the proportion and number of FoB cells (Figure 1C and D). Given the canonical and noncanonical contributions of Otub1 in regulating signaling pathways,²⁸ we queried which domain(s) of Otub1 participated in the regulation of splenic B cell maturation. First, we focused our attention on the catalytic domain of Otub1 by introducing the Otub1 C91S mutation into mice using CRISPR/Cas9-based genome editing and confirming germline transmission of the C91S mutation by sequencing (Supplementary material, Figure S1E). *Otub1^{C91S/C91S}* mice exhibited substantial prenatal lethality (data not shown), which precluded us from studying their B cells. To circumvent this problem, we crossed B-Otub1-fl/fl mice with *Otub1^{WT/C91S}* mice to generate *Mb1^{Cre/+}.Otub1^{C91S/fl}* (B-Otub1-C91S/fl) mice. Cre-mediated deletion or single base substitution (C91S) of one Otub1 copy did not impact splenic B cell maturation (Figure 1E and F). However, we noticed that Otub1 C91S mutation in B cell-specific Otub1 haplo-insufficient mice was sufficient to recapitulate the changes previously observed in splenic B cell subsets from B-Otub1-fl/fl mice (Figure 1E and F). In contrast, inactivation of Otub1 E2-binding site by mutating its T134 residue into arginine (T134R) (Supplementary material, Figure S1F), which interferes with the noncanonical function of Otub1,¹² did not alter splenic B cell maturation (Otub1-T134R, Figure 1G and H). Together, our data suggested that Otub1 contributes to the maturation of splenic B cells via its canonical DUB activity.

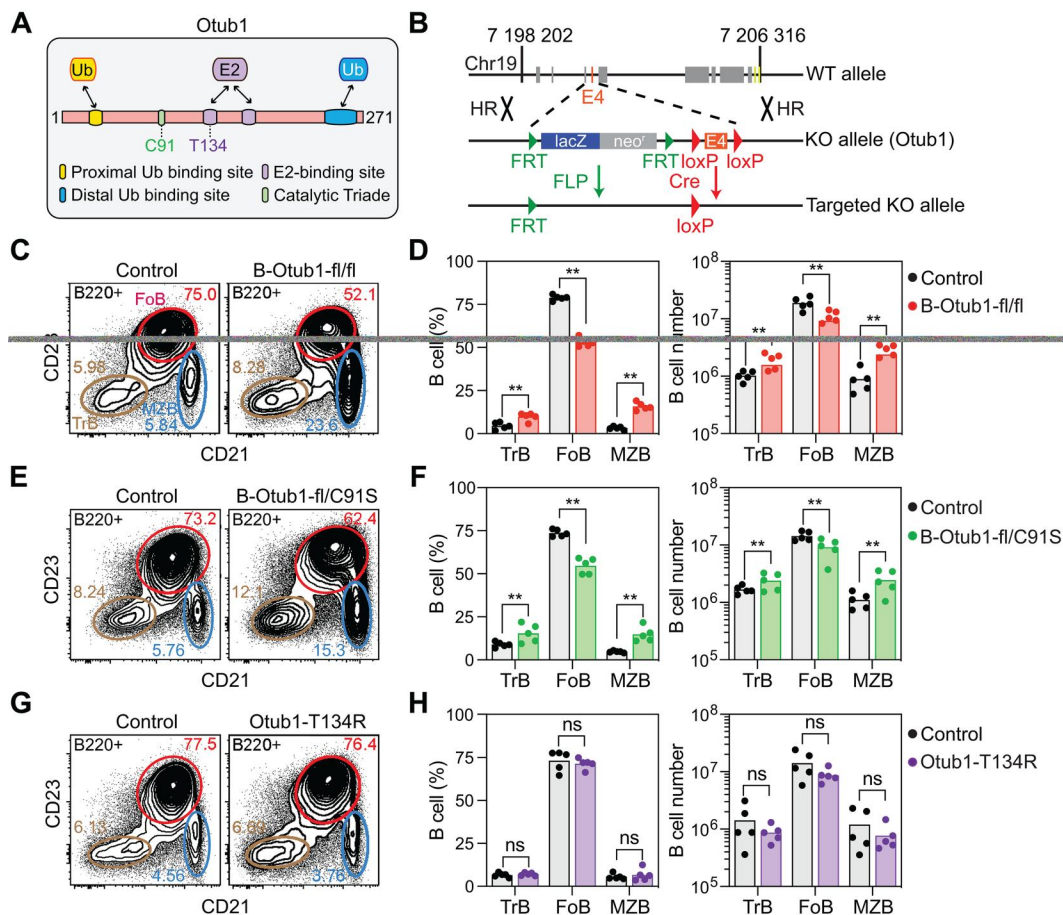


Figure 1 Splenic B cell subset representation is altered by *Otub1* deficiency. (A) Schematic of *Otub1* showing its major functional domains: C91 is part of the catalytic triad, T134 is part of the E2-binding domain. (B) Schematic representation of the gene targeting construct for deletion of exons 4–7 of *Otub1* and targeted deletion of *Otub1* exon 4. FRT: Flippase Recognition Target, FLP: Flippase. (C) Representative flow cytometry profile of B220⁺ splenic cells from control (*Otub1*^{fl/fl}) vs B-*Otub1*-fl/fl (*Mb1*^{cre/+}.*Otub1*^{fl/fl}) mice. The indicated numbers represent the percentages of CD21^{low}CD23^{low}B220⁺ TrB cells, CD21^{low}CD23^{high}B220⁺ FoB cells, and CD21^{high}CD23^{low}B220⁺ MZB cells. (D) Percentage and absolute number of B cell subpopulations in the spleen from control (*Otub1*^{fl/fl}) and B-*Otub1*-fl/fl (*Mb1*^{cre/+}.*Otub1*^{fl/fl}) mice. Values for individual mice (dots) and mean (bars) values are plotted (*n* = 5). (E) Representative flow cytometry analysis of B220⁺ splenic cells from control vs B-*Otub1*^{fl/fl}/C91S (*Mb1*^{cre/+}.*Otub1*^{fl/fl}/C91S) mice as in (C). (F) Percentage and absolute number of B cell subpopulations in the spleen from control and B-*Otub1*^{fl/fl}/C91S (*Mb1*^{cre/+}.*Otub1*^{fl/fl}/C91S) mice. Values for individual mice (dots) and mean (bars) values are plotted (*n* = 5). Control mice are either *Mb1*^{cre/+}.*Otub1*^{+/+}, *Otub1*^{+/+} or *Otub1*^{C91S/fl} mice. (G) Representative flow cytometry analysis of B220⁺ splenic cells from control vs *Otub1*^{T134R/T134R} mice as in (C). (H) Percentage and absolute number of B cell subpopulations in the spleen from control vs *Otub1*^{T134R/T134R} mice. Values for individual mice (dots) and mean (bars) values are plotted (*n* = 5). Control mice are either *Otub1*^{+/+} or *Otub1*^{T134R/+} mice. Significance was determined by unpaired *t* test. ***P* < 0.01; ns, nonsignificant.

Gng2 protein is stabilized by *Otub1* in splenic B cells

To gain better insight into how *Otub1* impacts B cell maturation, we used a mass-spectrometry (MS)-based proteomic approach and quantified substrates that were destabilized upon *Otub1* loss in splenic B cells. B220⁺ cells were purified from both Cre-negative control and B-*Otub1*-fl/fl mice and differentially expressed proteins were evaluated by MS. In total, we detected 1,834 proteins in Cre-negative control and B-*Otub1*-fl/fl conditions combined, out of which only five were decreased by more than 2-fold in B-*Otub1*-fl/fl B220⁺ B cells (Figure 2A, Supplementary material, Table S1). Both *Otub1* itself and the E2 ubiquitin conjugating enzyme Ube2k,²⁹ were among the differentially expressed proteins, thereby validating our MS-based quantification approach. Interestingly, the γ -subunit Gng2 of the heterotrimeric G protein emerged as one of the most decreased proteins in this analysis, with a 5.3-fold decrease in B-*Otub1*-fl/fl relative to control B cells. Importantly, we confirmed that the decrease in Gng2 protein levels was not a result of changes in

transcript expression by quantifying *Gng2* mRNA levels (Supplementary material, Figure S2A).

Gng2 is one of 12 known γ -subunits that comprise the heterotrimeric guanine nucleotide binding ($G\alpha\beta\gamma$) complex,^{30,31} which is critical for relaying information between GPCRs and intracellular effectors.³² Of note, a previous study identified a SNP in the 3'-UTR of GNG2 as being associated with a higher risk of developing IgA nephropathy,³³ suggestive of a potential role of GNG2 in B cells. In fact, we observed that adult B-*Otub1*-fl/fl mice displayed a significant increase in serum and fecal IgA levels (Supplementary material, Figure S2B). The Immunological Genome Project (Immgen) consortium has reported mRNA sequencing gene expression profiles of multiple murine B cell subsets and analysis of the 12 γ -subunits showed that *Gng2* is the most abundantly expressed subunit in the TrB, FoB and MZB cell subsets in the spleen (Supplementary material, Figure S2C).³⁴ Of note, Gng2 was the only γ -subunit protein that was detected in our MS analysis. We therefore focused our attention towards validating Gng2 as a substrate of *Otub1* for further study.

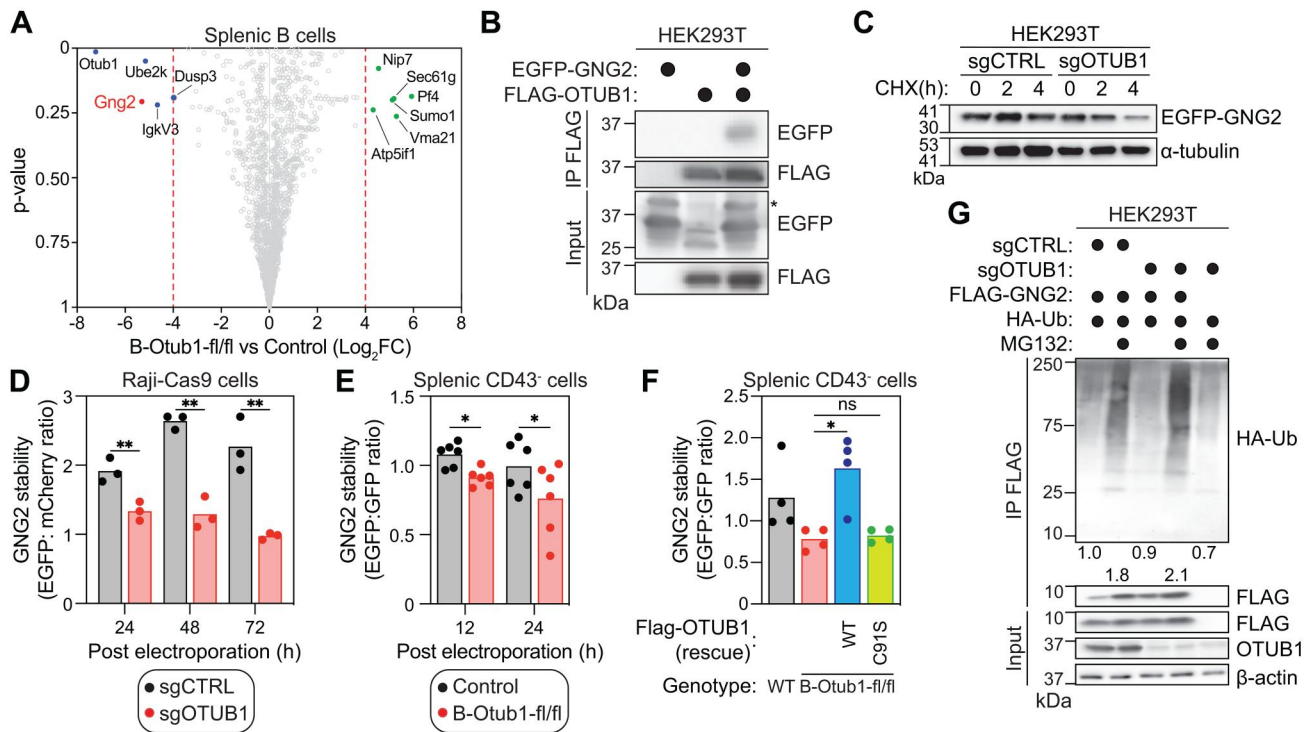


Figure 2 Otub1 regulates Gng2 stability *in vivo* and *in vitro*. (A) Relative protein abundance of B220⁺ B-Otub1-fl/fl cells compared with control versus statistical significance with Log₂FC > 4 proteins highlighted (n = 3). (B) HEK293T cells were transfected with FLAG-OTUB1 and EGFP-GNG2 expression vectors as indicated. Forty-eight hours posttransfection, cells were lysed and Otub1 complexes were immunoprecipitated using anti-FLAG (M2) resin and then analyzed by immunoblotting using GFP and FLAG antibodies (n = 5). (C) Representative blots of *in vitro* cycloheximide (CHX) chase assays to detect GFP protein expression level in immunoprecipitates from sgCTRL or sgOTUB1 HEK293T transfected with EGFP-GNG2 at 0, 2, and 4 h. Forty-eight hours after transfection, cells were treated with CHX (100 μg/mL) for indicated times before cell collection (n = 3). (D) sgCTRL or sgOTUB1 Raji-Cas9 cells were electroporated with EGFP-GNG2 or mCherry constructs and the ratio of EGFP to mCherry signal at the indicated timepoints were plotted (n = 3). Statistical analyses were performed using Wilcoxon signed-rank test. **P < 0.01. (E) CD43⁺ splenic cells from control or B-Otub1-fl/fl mice were electroporated with EGFP-GNG2 or GFP constructs and the ratio of EGFP-GNG2 to GFP signal at the indicated timepoints were plotted (n = 6). Statistical analyses were performed using Wilcoxon signed-rank test. *P < 0.05. (F) CD43⁺ splenic cells from control or B-Otub1-fl/fl mice were electroporated with EGFP-GNG2 constructs and indicated rescue constructs. The ratio of EGFP to GFP signal at 12 h were plotted (n = 4). Statistical analyses were performed using Kruskal–Wallis ANOVA. ns, nonsignificant. (G) Representative blots of *in vitro* ubiquitylation assays of input and immunoprecipitates from sgCTRL or sgOTUB1 HEK293T cells transfected with plasmids expressing indicated proteins. Forty hours after transfection, cells were treated with MG132 (20 μM) for 8 h before cell collection. Relative densitometry values given below each lane relative to sgCTRL HEK293T cells. HA-Ub, HA-tagged ubiquitin (n = 5).

First, we tested whether Otub1 directly interacts with its substrate Gng2 to prevent its ubiquitylation and hence its subsequent degradation. We transiently expressed tagged versions of both human OTUB1 and GNG2 in HEK293T cells and performed coimmunoprecipitation experiments. We detected the presence of EGFP-GNG2 in our pulldown of FLAG-tagged OTUB1 (Figure 2B), providing evidence of a physical association of GNG2 with OTUB1. To functionally validate the relevance of OTUB1-GNG2 interaction, we investigated the impact of OTUB1 depletion on GNG2 stability *in vitro* in both human and murine cell lines. The absence of a specific antibody recognizing either human or mouse GNG2 precluded us from studying endogenous levels by immunoblot. Instead, we conducted a cycloheximide (CHX) chase assay to examine EGFP-GNG2 protein half-life in both control (sgCTRL) and OTUB1-depleted (sgOTUB1) HEK293T cells (Supplementary material, Figure S2D). Strikingly, lack of OTUB1 significantly impaired EGFP-GNG2 protein stability 4 h post-CHX treatment compared to control conditions (Figure 2C, Supplementary material, Figure S2E). We extended our analysis to the human Raji B cell-derived Burkitt's lymphoma cell line where EGFP-GNG2 was transiently expressed in presence (sgCTRL) or absence of OTUB1 (sgOTUB1) (Supplementary material, Figure S2F and G). Here, we monitored EGFP-GNG2 levels by flow

cytometry over 72 h using an mCherry construct as a normalizing control. In line with our previous observations, the ratio of EGFP-GNG2/mCherry was significantly lower in OTUB1-depleted Raji cells compared to control (Figure 2D). Similarly, relative EGFP-GNG2 levels were consistently and significantly decreased 12 h and 24 h postelectroporation in splenic CD43⁺ B cells extracted from B-Otub1-fl/fl mice compared to controls (Figure 2E, Supplementary material, Figure S2H), supporting a role for Otub1 in promoting Gng2 protein stability in B cells. Importantly, EGFP-GNG2 levels were rescued in B-Otub1-fl/fl CD43⁺ B cells upon re-expression of wild-type (WT) but not C91S OTUB1 (Figure 2F, Supplementary material, Figure S2I), confirming the importance of OTUB1 DUB activity in the stabilization of GNG2. As such, we reasoned that OTUB1 cleaves polyUb chains on GNG2 to promote its stability, and therefore monitored changes in GNG2 ubiquitylation status upon depletion of OTUB1 in HEK293T cells. As expected, inhibition of the proteasome with MG132 (20 μM, 8 h) led to a significant accumulation of FLAG-tagged GNG2 polyubiquitylated forms compared to control conditions (Figure 2G, Supplementary material, Figure S2J). Taken together, our data support a model where OTUB1 stabilizes GNG2 protein levels in both murine and human cells by modulating the ubiquitylation of GNG2.

Otub1 loss results in hyperresponsive chemokine receptor signaling in B cells

To investigate how the OTUB1-GNG2 signaling axis might play a role in mature B cells, we mapped GNG2's proximal interactome in HEK293T cells using the BioID approach.³⁵ Proteins that are in close proximity to the BirA-tagged construct of GNG2 are biotinylated and subsequently pulled down with streptavidin before being subjected to MS analysis (Supplementary material, Figure S3A). As would be expected, we identified several subunits of the heterotrimeric G protein, including alpha (GNA11, GNA13, GNA13, GNAI1-3, GNAO1, GNAQ, GNAS and GNAZ) and beta subunits (GNB1, GNB4) (Supplementary material, Figure S3B, Table S2), thereby confirming the validity of our approach. Probing the proximal interactome of GNG2 also identified several biological pathways and complexes which included, among others, proteins involved in the actin cytoskeleton (JUP, MARCKS, CASK; $P = 8.34 \times 10^{-16}$), cell migration (PHACTR4, JUP, DDRGK1; $P = 7.37 \times 10^{-12}$), chemokine signaling (ROCK1, GNB1, GNB4; $P = 0.0017$), calcium signaling (STIM1, VDACC1, ITPR2; $P = 0.0036$) and mTORC2 signaling (RICTOR, MAPKAP1; $P = 0.0256$) (Figure 3A, Supplementary material, Table S3).

Chemokine signaling is initiated upon ligand-receptor binding and the activation of the receptor-associated $G\alpha$ and $G\beta\gamma$ subunits of the heterotrimeric G proteins. This is followed by a series of secondary messengers, including the release of Ca^{2+} from intracellular stores, a remodeling of the actin cytoskeleton and the regulation of the mechanistic Target of rapamycin (mTOR) pathway.³⁶ The GPCRs Cxcr4, Cxcr5 and S1pr1, and their corresponding chemokines ligands Cxcl12, Cxcl13 and S1P respectively, play a major role in the maturation of splenic B cells.³⁷⁻³⁹ Given the importance of chemokines in splenic B cell localization, we therefore asked whether Otub1-deficient murine B cells, through the reduced stability of Gng2, displayed aberrant chemokine-specific GPCR activation. First, we measured Ca^{2+} signaling in both MZB and FoB cells upon stimulation with two chemokines, Cxcl12 and Cxcl13. Interestingly, we observed a significantly greater Ca^{2+} mobilization upon Cxcl12 stimulation in both primary FoB and MZB cells obtained from B-Otub1-fl/fl mice compared to WT controls (Figure 3B and C). We therefore extended our analysis to 2PK-3 cells where Otub1 and Gng2 can be targeted by CRISPR technology (Supplementary material, Figure S3C and D). Indeed, targeting Otub1 in 2PK-3 cells led to an increased mobilization of cytosolic Ca^{2+} upon stimulation with Cxcl12, compared to control cells (Figure 3D). Similarly, significantly greater Ca^{2+} flux was observed in Gng2-depleted 2PK-3 cells upon stimulation with Cxcl12 (Figure 3D). These observations led us to ask whether Otub1-Gng2 interaction may be impacted by chemokine stimulation. We therefore transiently expressed tagged versions of both human OTUB1 and GNG2 in 2PK-3 cells and performed coimmunoprecipitation experiments at different time points post-Cxcl12 stimulation. Interestingly, OTUB1-GNG2 interaction remained unchanged upon chemokine stimulation (Supplementary material, Figure S3E), suggesting a constitutive association of OTUB1 with GNG2.

Together with other GPCR-induced signaling events, intracellular Ca^{2+} signaling controls a series of cellular processes, including proliferation and differentiation, cellular motility, and metabolism.⁴⁰ This latter process is coordinated by mTOR and its two distinct protein complexes, mTORC1 and mTORC2,⁴¹ in part by the association of mTOR with different $G\beta\gamma$ heterodimers.⁴² As such, we reasoned that Otub1, through regulating Gng2, could result in increased mTOR activation. To determine whether this was the case, we measured phosphorylation levels of RPS6 (p-RS6), a downstream effector of the mTOR signaling pathway, by flow cytometry in control and B-Otub1-fl/fl B cells after Cxcl12 stimulation. Our data showed that Cxcl12 stimulation led to an increase in p-RS6 levels that were present for longer in B-Otub1-fl/fl B cells than in WT cells (Supplementary material, Figure S3F).

Aside from mTOR signaling, it has previously been shown that chemokine engagement can result in F-actin polymerization as cells polarize in the direction of the chemokine, hence initiating chemotaxis.⁴³ To corroborate our Ca^{2+} flux data, we therefore measured F-actin levels in splenic B cells after Cxcl13 stimulation using phalloidin staining. Strikingly, we observed a sustained increase in Cxcl13-dependent actin polymerization both in FoB and MZB cells from B-Otub1-fl/fl mice (Figure 3E, Supplementary material, Figure S3F). Finally, to test whether the increased chemokine receptor signaling in Otub1-deficient B cells was translated into an increased functional responsiveness to homeostatic chemokines, we utilized the transwell assays to assess FoB and MZB cell chemotaxis.⁴⁴ We found that there was significantly more chemotaxis of FoB and MZB cells in response to Cxcl12, Cxcl13 or S1p, when they lacked Otub1, compared to their WT counterparts (Figure 3F). To determine whether this phenotype was the result of a difference in the GPCR surface expression, we examined Cxcr4, Cxcr5 and S1pr1 levels on FoB and MZB cells both from B-Otub1-fl/fl and control mice. Although we noted some minor changes in their expression (FoB cells: up to +1.3-fold; MZB cells: -1.1-fold), these changes were unlikely to account for the hyperresponsiveness observed in both FoB and MZB cells from B-Otub1-fl/fl mice (Supplementary material, Figure S3H and I). Altogether, our data strongly suggested that Otub1 loss led to hyperactivated GPCR signaling and chemokine responsiveness via the increased stability of Gng2.

Single cell analyses delineated transcriptionally indistinguishable but differentially localized splenic B cell subsets

Triggering GPCR signaling through their associated G-coupled proteins ultimately leads to changes in gene expression.⁴⁵ Thus, we wondered whether the Otub1-mediated hyperresponsiveness to the different chemokines that we tested *in vitro* resulted in transcriptional changes in splenic B cell subsets or in their differentiation trajectories *in vivo*. We set out to answer this question by performing a single cell RNA sequencing (scRNA-seq) analysis of B220⁺ splenic B cell both from control and B-Otub1-fl/fl mice. A total of 14,568 cells were retained after quality control filtering that were

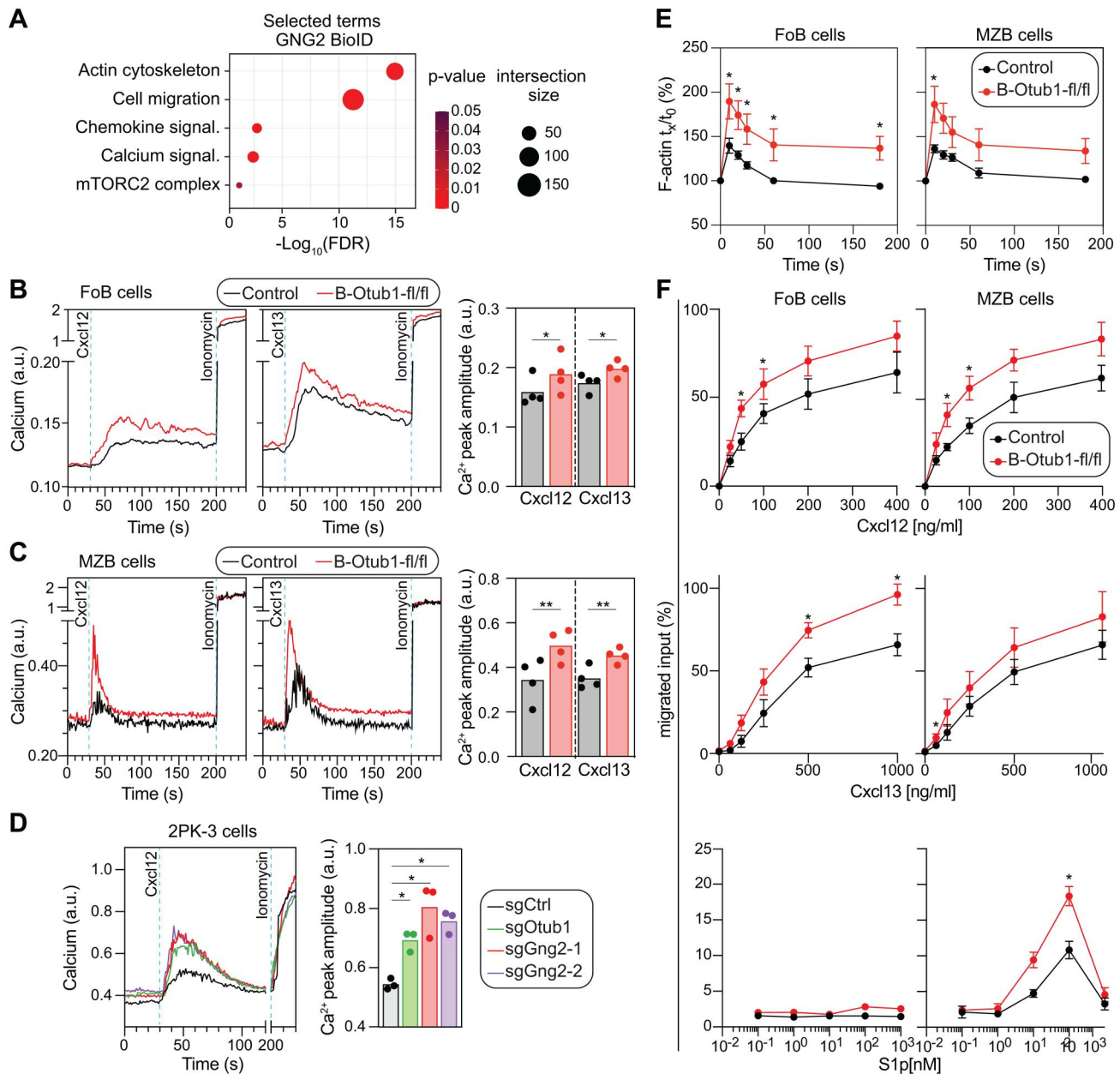


Figure 3 Otub1 loss results in increased calcium signaling, actin polymerization and chemotaxis in B cells. (A) Selected enriched GO terms were identified using g:Profiler (adjusted $P < 0.05$, with Benjamini–Hochberg FDR correction). Circle size indicates the number of proteins from the GNG2 interactome that intersects with each term, x-axis position indicates $-\log_{10}$ -transformed FDR score and colors indicate the fold enrichment. (B) FoB cells from control and B-Otub1-fl/fl were stained with Indo-1 and the ratio of Ca²⁺-bound Indo-1 to Ca²⁺-unbound Indo-1 was measured by flow cytometry before and after stimulation with the indicated chemokines (Cxcl12, 100 ng/mL; Cxcl13, 500 ng/mL). Ionomycin (500 ng/mL) was used as a positive control (left). Graph summarizing the peak Ca²⁺ amplitude after Cxcl12 or Cxcl13 stimulation ($n = 4$) (right). Statistical analyses were performed using paired one-tailed Student's t -test. * $P < 0.05$. (C) Same as in (B) except that FoB cells were replaced by MZB cells (left). Graph summarizing the peak Ca²⁺ amplitude after Cxcl12 or Cxcl13 stimulation ($n = 3$) (right) ($n = 4$). Statistical analyses were performed using paired one-tailed Student's t -test. **, $P < 0.01$. (D) Cells were similarly stained as in (B) except that primary B cells were replaced with 2PK-3 cells targeted with indicated sgRNA and stimulated with Cxcl12 (200 ng/mL). Ionomycin (200 ng/mL) was used as a positive control (left). Accompanying summary graph of the peak calcium amplitude after Cxcl12 stimulation ($n = 3$) (left) or MZB (right) cells were exposed to Cxcl13 (1000 ng/mL) for various times and the F-actin levels were determined by flow cytometry analysis of phalloidin stained cells. F-actin content is expressed as a fraction of baseline untreated control B cells. Data are from three independent experiments with two WT and two B-Otub1-fl/fl mice per experiment. (E) Chemokine or Sphingosine-mediated ex vivo B cell transwell assay. Control or B-Otub1-fl/fl splenic cells were placed in transwell chambers and response towards Cxcl12 ($n = 5$), Cxcl13 ($n = 3$), or S1p ($n = 3$) concentrations was measured. Data are presented as the per cent of input cells that migrated to the lower chamber during the 3-h assay. Data represents \pm SEM. Significance was determined using a one-way ANOVA with Tukey's multiple test comparisons (D) or two-way ANOVA with Holm–Sidak's test (E, F). * $P < 0.05$; ns, nonsignificant.

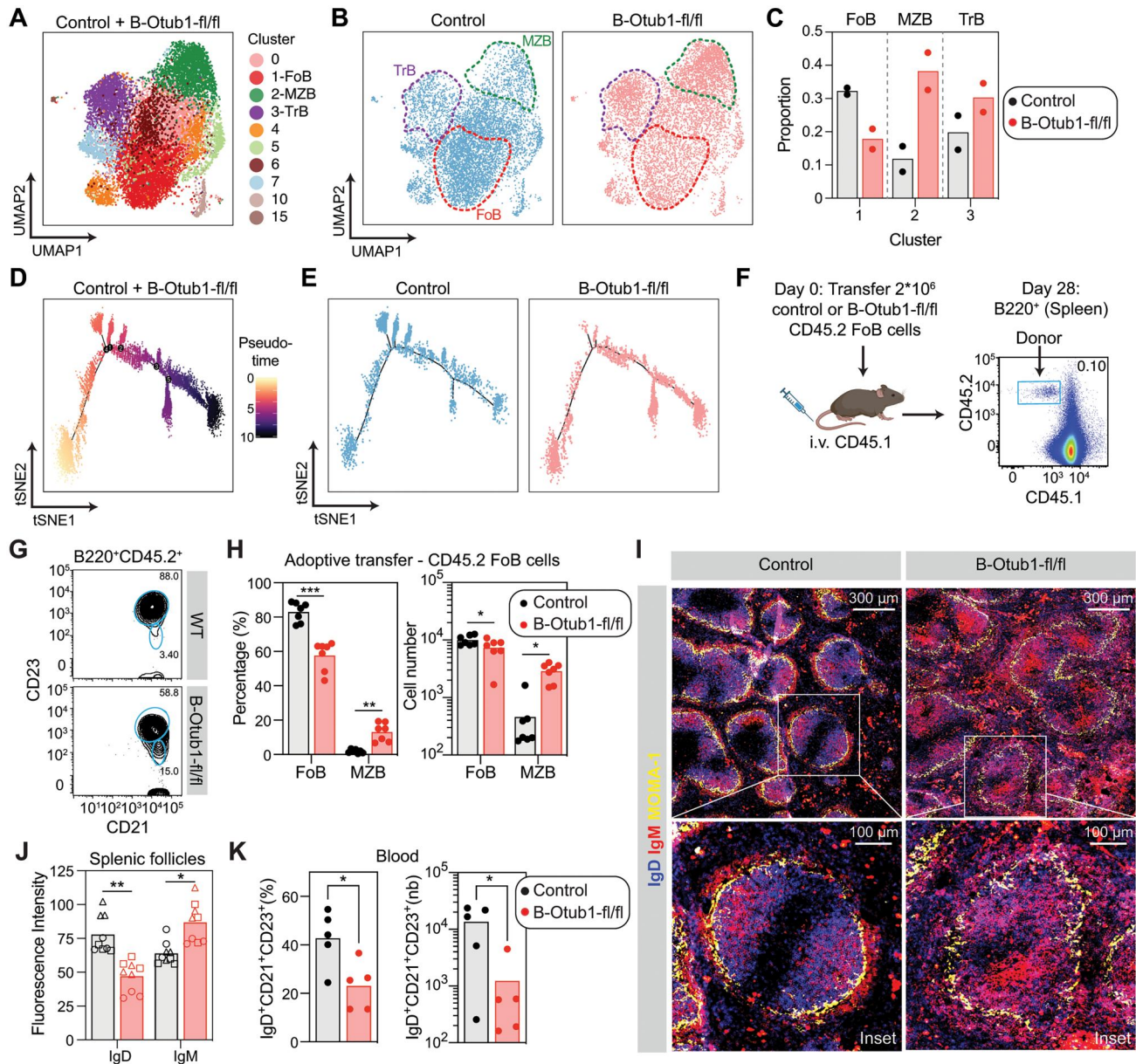
analyzed using unsupervised graphical clustering and visualized using uniform manifold approximation and projection (UMAP). Combined clustering identified a total of 16 clusters, of which 10 were comprised of B cells, as determined by

their expression of *cd19*, *cd79a* and *cd20* (Cluster 0–7, 10 & 15; 13,712 cells), and 6 were non-B cells clusters (Cluster 8, 9, 11–14; 856 cells), which were excluded from further analyses (Figure 4A, Supplementary material, Figure S4A). Of note, the

presence of the non-B cell clusters (~6% of captured cells in the dataset) was consistent with the purity obtained post-magnetic sorting.

To determine the identity of the largest UMAP clusters, we used publicly available microarray and RNA-seq datasets,^{46,47} extracted gene signatures from different splenic B cell subtypes and organized them into six distinct gene ontology pathways to project them across our scRNA-seq

dataset using single-sample gene set enrichment analysis (ssGSEA) (Supplementary material, Figure S4B). This analysis allowed us to assign cluster 1 as FoB cells, cluster 2 as MZB cells, and cluster 3 as TrB cells (Figure 4A). Of note, the proportion of B cells within these three clusters closely mirrored our flow cytometry data, with increased frequencies of TrB and MZB cells and decreased frequencies of FoB cells observed upon loss of *Otub1* (Figure 4B and C). Importantly,



aside from differences in frequency, we did not detect any significant transcriptional differences in these three defined B cell subsets between control and B-Otub1-fl/fl mice. Out of the 13,146 protein-coding genes detected by scRNA-seq, <0.0026% (34 genes) were differentially expressed ($\text{Log}_2\text{FC} \pm 0.25$, P -adjusted value < 0.05) when cells from control mice were compared to those extracted from B-Otub1-fl/fl in clusters 1 to 3 (Supplementary material, Table S4). In addition, we performed a trajectory analysis to capture the putative transcriptional dynamics underlying the differentiation of B cells (Figure 4C). Our pseudo-time reconstruction defined a transcriptional gradient starting from TrB cells, progressing towards FoB, and terminating with MZB cells (Figure 4D, Supplementary material, Figure S4C). This suggested that MZB cells could be derived from FoB cells, consistent with previous reports.⁴⁸ Importantly, the scRNA-seq pseudo-time analysis revealed similar developmental trajectories of splenic B cells isolated from control compared to B-Otub1-fl/fl mice (Figure 4E). Altogether, these data suggested that loss of Otub1 resulted in limited transcriptional changes and differentiation trajectories in splenic B cells as compared to their WT counterparts.

To test whether there was increased differentiation of MZB cells originating from FoBs in Otub1-deficient mice, as our scRNA-seq trajectory analysis suggested, we sorted B220⁺CD21⁺CD23⁺ FoB cells from CD45.2⁺ control or B-Otub1-fl/fl mice and adoptively transferred them into CD45.1⁺ WT recipients (Figure 4F). While adoptively transferred WT FoB cells showed minimal differentiation into MZB cells 28 days post-transfer (Figure 4G and H), we noted a striking 7-fold increase in the percentage of MZB cells that emerged from adoptively transferred Otub1-deficient FoB cells, which translated into a ~6-fold increase in the total number of MZB cells (Figure 4G and H). These findings suggested that Otub1-deficient splenic FoB cells have a greater propensity to differentiate into MZB cells, in line with our scRNA-seq data.

Several chemokines receptors, including Cxcr4, Cxcr5 and S1pr1, have been previously shown to control the maturation of FoB into MZB cells by governing both the positioning of different B cell subsets as well as their migration between the distinct areas in the spleen.^{37–39} We therefore assessed the presence and localization of splenic B cells by confocal microscopy. We stained sections of the spleen for MOMA-1, a marker of marginal metallophilic macrophages, to delineate the MZ, and combined to IgM and IgD staining in order to monitor MZB and FoB cells, respectively, within the spleen. Strikingly, the white pulp B cell follicles appeared considerably more disorganized in absence of Otub1 expression (Figure 4I). Consistent with our flow cytometry data that showed a reduction in the number of FoB cells, we observed a significant decrease in IgD⁺ fluorescence intensity within the splenic follicles of B-Otub1-fl/fl mice compared to control (Figure 4J). Interestingly, the distribution of IgM⁺ MZB cells was not limited to the marginal zone (Figure 4I), and we noticed a significant increase in IgM fluorescence intensity within the follicles delineated by MOMA-1 staining (Figure 4J). Of note, we observed no difference in IgM or IgD surface expression between WT and Otub1-deficient splenic B cells by flow cytometry (data not shown). Together, these data

suggested that loss of Otub1 impaired the localization of IgM⁺ MZB cells within the spleen.

Given that the same chemokines found in the spleen (Cxcl12, Cxcl13 and S1p) also determine the positioning of B cells in lymph nodes, as well as the trafficking of FoBs between blood and secondary lymphoid organs,^{37,38,49,50} we extended our analyses to lymph nodes and the blood. While we did not observe any significant differences in number or location of B cells in the lymph nodes in comparing WT and B-Otub1-fl/fl mice (Supplementary material, Figure S4D and E), when we quantified the presence of IgD⁺CD21⁺CD23⁺ mature circulating B cells within the blood we noted a significant decrease (~2-fold decrease by percentage; ~10-fold decrease in absolute number) in circulating FoB cells in B-Otub1-fl/fl mice compared to WT mice (Figure 4K, Supplementary material, Figure S4F). Jointly, our data suggested that Otub1 deficiency, through hyperresponsive chemokine receptor signaling, may alter splenic B cell positioning and trafficking, which in turn impact B cell maturation within the spleen.

Discussion

Our study revealed that the DUB Otub1 is a modulator of chemokine receptor signaling in B cells. Indeed, Otub1 deficiency led to a hyperresponsiveness of B cells to homeostatic chemokines *in vitro* and an altered positioning of MZB cells within the spleen *in vivo*, while having little impact on B cell development in the BM. Our proteomics-based analysis identified Gng2 as a novel substrate of Otub1, suggesting that Otub1 modulates B cell chemotaxis and trafficking by stabilizing this γ -subunit of the heterotrimeric G protein. Together, our study adds to a body of work highlighting the importance of fine-tuning GPCR signaling in B cells and identifies a role for deubiquitylating events in this process.

Of the heterotrimeric G protein subunits α , β and γ , all G α subunits, except G α 12/13, were previously shown to be ubiquitylated⁵¹; however, examples of functional ubiquitylation of either G β or G γ subunits have been rare.^{52–55} Interestingly, previous work has shown that the γ -subunit GNG2 can be ubiquitylated as part of the transducin receptor, thereby destabilizing its association with the G β subunit and modulating GPCR signaling.^{54,55} To the best of our knowledge, no deubiquitylation events have so far been reported to control any heterotrimeric G protein subunits. We demonstrated, for the first time, that Gng2 is a substrate of the deubiquitylase Otub1 in higher eukaryotes, a process that we showed was needed for the modulation of chemokine receptors in murine B cells. Controlling the stability of the heterotrimeric G proteins through ubiquitylation/deubiquitylation events may provide an important negative feedback mechanism to limit the activation and deactivation steps of GPCR signaling. Indeed, we observed a significant mobilization of cytosolic Ca²⁺ in response to chemokine stimulation upon loss of Gng2 or Otub1 in 2PK-3 cells, suggesting a role for the Otub1-Gng2 axis in the negative control of GPCR signaling. It could also modify the stoichiometry of the different subunits of the heterotrimeric G proteins, thereby favoring the association of distinct α , β and γ subunits to enable the fine-tuning

of chemokine signaling. However, how this posttranslational regulation of chemokine signaling translates into the altered positioning of splenic B cells that we observed *in vivo*, remains an open question.

Multiple signaling inputs have been shown to promote the maturation of FoB into MZB cells, including BCR signal strength, NF- κ B-mediated BAFF signaling and Notch2 activation.¹⁸ Our preliminary data suggested that Otub1 had limited impact on these signaling pathways *in vitro* (data not shown). The chemotactic response of splenic B cells was the only major feature that was drastically affected by the loss of the DUB Otub1. Our current working model is that the regulation of Gng2 stability in splenic B cells results in a hyperresponsiveness to chemokines both *in vitro* and *in vivo*, which in turn affects their localization/retention within the MZ and their maturation into MZB cells. While we cannot exclude that Otub1 may modulate the stability of additional substrates linked to B cell development, previous studies have shown that targeting intracellular GPCR effectors of the G protein α inhibitory subunits (e.g., *G α 2* and *G α 3*) resulted in a defect in both the maturation and the localization of murine splenic B cells,^{56,57} in line with our findings. Importantly, the chemokine signaling hyperresponsiveness that we observed in Otub1-deficient B cells had minimal transcriptional impact when measured by scRNAseq, but rather increased the capacity of Otub1-deficient FoB cells to give rise to MZB cells, highlighting the fundamental contribution of chemokine signaling in the regulation of splenic B cell fate.

It is already well established that targeting chemotactic GPCRs can significantly alter B cell positioning within the splenic white pulp and impact their cell fate. For instance, loss of *Cxcr5*, which is upregulated after B cell egress from the BM,⁵⁸ promoted the development of IgM⁺ MZB cells and resulted in the failure of IgD⁺ FoB cells to properly localize within the splenic follicles.³⁸ Moreover, targeting *S1pr1*, whose expression increases as differentiation of B cells progresses in the BM and the spleen,⁵⁹ favored the development of MZB cells at the expense of FoB cells and *S1pr1*-deficient MZB cells failed to localize within the MZ of the spleen.³⁹ Targeting G-protein linked chemoattractant receptors had a similar effect on B cell positioning and maturation: lack of *G α 2* or *G α 3* in B cells resulted in a reduced response to chemo-attractants *in vitro*,^{57,60} while *G α 2* or *G α 3*-deficient mice displayed significantly less MZB cells as well as smaller B cell follicles within the spleen,⁵⁷ highlighting the role of chemotactic GPCRs and their associated G proteins in the positioning of B cells within the spleen. However, it remains to be determined whether targeting *Gng2* in B cells may recapitulate the same key features that we observed in our B-Otub1-fl/fl mice.

In conclusion, our findings suggest that regulating chemotactic GPCR signaling through ubiquitylation/deubiquitylation is a mechanism by which splenic B cells may rely upon to regulate both their positioning *in situ* and cell fate decision. In this study, we identified *Gng2* as a target of the UPS, thereby emphasizing the contribution of this dynamic post-translational modification in the regulation of chemotactic responses and the fine-tuning of GPCR-associated biological effects.

Materials and Methods

Mice

Otub1-fl/fl mice were generated as described previously⁶¹ with two loxP sites flanking exon 4 of Otub1. Otub1^{+/-} mice were crossed with FLP/O mice (Jax Strain#003946) to remove the neomycin cassette resulting in a floxed allele. The progeny was assessed for germline transmission and subsequently used at the age of 8–12 weeks unless otherwise stated. Mb1^{Cre/+} mice were a gift from Dr Michael Reth (University of Freiburg, Germany). CD45.1⁺ congenic B6 mice were a gift from Dr Francois Mercier (McGill University, Canada).⁶² Otub1^{C91S/+} and Otub1^{T134R/+} point mutation mice were generated using a CRISPR-Cas9 genome-editing at the TCP mouse facility (University of Toronto, Canada). The sequence 5'-AACTGCTTCTACCGAGCGTTTGG-3' was selected as the target for single guide RNA (sgRNA). A 117-nt single-stranded oligodeoxynucleotide (ssODN) donor coding the Otub1 C91S or T134R mutation was ordered as Ultramer DNA oligos from Integrated DNA Technologies (Skokie, IL, USA). The Cas9 mRNA, sgRNA, and ssODN were dissolved in nuclease-free water and microinjected into the cytoplasm of pronuclear-stage mouse zygotes obtained from C57BL/6Njcl mice (University of Toronto, Canada). The genotype was determined by PCR analysis using genomic DNA derived from the mice with the mouse Mb1 cre (forward primer sequence: 5'-GCTGATGGGAAGTCAAGCGAC-3', 5'-CCCTGTGGATGCCACCTC-3' & reverse 5'-GGGAACTGCTGAACCTTCTGTG-3', 5'-GTCCTGGCATCTGTGAGAG-3'); Otub1 floxed allele (forward primer sequence: 5'-TCCACCCCTTCATCTGCTTCT-3', and reverse primer sequence: 5'-CAGACCAGAGCAGGATTAAGAAGCCTA-3'); Otub1 C91S (forward primer sequence: wt 5'-CGTTTGTCTTCTTGCATTA-3' and mutant 5'-GGCCTGATGGCAACTC-3'; reverse primer sequence: wt/mutant 5'-GAAGGAATGGGAAGCCAATA-3'); and mouse Otub1 T134R (forward primer sequence: wt 5'-CCTTCATGAGGAAGTC-3' and mutant 5'-GGCTTCACTGAATTCAC/G-3'; reverse primer sequence: wt 5'-GTGGAAGTCTTCAATTG-3' and mutant 5'-GATAAGGTCCATGAACTGC-3'). Males and females were used in experiments in approximately equal ratios. Unless otherwise stated, all mice used were 8–12 weeks old. Transgenic mice were bred and maintained in the animal facility of the Lady Davis Institute of Medical Research (LDI), Jewish General Hospital in single ventilated cages. All animal experiments were performed in accordance with Animal Care Committee at the LDI and McGill University and followed the guidelines of the Canadian Council on Animal Care (CACC).

Flow cytometry

Cells were filtered through a 70 μ m nylon mesh to obtain single cell suspensions and subjected to red blood cell (RBC) lysis using RBC lysing buffer (Sigma). Cells were re-suspended in FACS buffer (D-PBS, 1% FBS, 2 mM EDTA, 0.05% Na₃N), stained with live/dead for 20 min on ice, then CD16/32 (BD) to block binding of Fc receptors for 20 min on ice. Cell surface antigens were subsequently stained for 20 min on ice in FACS buffer. Cells were analyzed unfixed or fixed at 4%

paraformaldehyde for 15 min for further analysis. Flow cytometry data was either recorded on an LSRFortessa (Becton Dickinson) or ID7000 spectral cell analyzer (Sony) and analyzed using FlowJo software (Tree Star). The list of antibodies used, and its corresponding clones can be found in [Table S5 \(Supplementary material\)](#).

RNA isolation and real time PCR

RNA was prepared using TRIzol Reagent (Invitrogen) according to manufacturer's instructions. Total extracted RNA was treated with DNaseI (Invitrogen) according to manufacturer's instructions. Complementary DNA was synthesized with LunaScript RT SuperMix Kit (NEB). qPCR was performed using universal Luna Universal qPCR Master Mix system (NEB) on an Applied Biosystems 7500 Fast Dx Real time PCR instrument. Gene transcript numbers were standardized and adjusted relative to GAPDH transcripts. The primer sequences are shown in [Table S6 \(Supplementary material\)](#).

Western blotting analysis

The NuPAGE electroblots were lysed in 1× NuPAGE buffer without dye (106 mM Tris-HCl, 141 mM Tris base, 2% LDS, 10% glycerol, 0.51 mM EDTA) supplemented with 1× protease inhibitors (Roche). Protein concentrations were determined using Pierce BCA protein assay kit (ThermoFisher). Protein dye was subsequently added to a concentration of 0.22 mM G250 Coomassie Blue, 0.175 mM Phenol Red; pH 8.5. Total protein lysates were resolved by NUPAGE Bis-Tris gel, transferred to 0.45 μM PVDF membranes (GE), probed with indicated antibodies and visualized with an Amersham ECL Prime Western blotting Detection kit (GE Healthcare). A complete list of antibodies used can be found in [Table S5 \(Supplementary material\)](#).

Mass spectrometry of B220⁺ murine splenocytes

Splenic cells were prepared as described above. In addition, B cells were enriched by staining with B220⁺ MACS beads (Miltenyi Biotech) and passed through a Miltenyi LS column according to manufacturer's suggestion. Cells were lysed in high salt lysis buffer (50 mM Tris, 300 mM NaCl, 1 mM EDTA, 1% Triton X-100). For each sample, mouse spleen lysates were loaded onto a single stacking gel band to remove lipids, detergents, and salts. The single gel band containing all proteins was reduced with dithiothreitol (DTT), alkylated with iodoacetic acid, and digested with trypsin. A 2-μg aliquot of the extracted peptides was resolubilized in 0.1% aqueous formic acid and loaded onto a Thermo Fisher Acclaim Pepmap (Thermo Fisher Scientific, 75 μM ID × 2 cm C18 3 μM beads) precolumn and then onto an Acclaim Pepmap Easyspray (Thermo Fisher, 75 μM × 15 cm with 2 μM C18 beads) analytical column separation using a Dionex Ultimate 3000 UHPLC at 250 nL/min with a gradient of 2–35% organic (0.1% formic acid in acetonitrile) over 3 h. Peptides were analyzed using a Thermo Orbitrap Fusion mass spectrometer operating at 120,000 resolution (FWHM in MS1) with higher-energy C-trap

dissociation (HCD) sequencing (15,000 resolution) at top speed for all peptides with a charge of 2+ or greater. The raw data were converted into *.mgf format (Mascot generic format) for searching using the Mascot 2.6.2 search engine (Matrix Science) against mouse protein sequences (Uniprot2019). The database search results were loaded onto Scaffold Q+ Scaffold_4.9.0 (Proteome Sciences) and exported to GraphPad Prism v9 for statistical treatment and visualization ([Supplementary material, Table S1](#)). Proteins that were not detected with in at least two replicates of one condition were removed. From the remaining list, proteins that did not have at least three peptide-spectrum-matches (PSM) in at least one replicate were removed as well. Next, normalized spectral abundance factors (NSAF) were calculated for each protein and sample based on its number of PSM and molecular weight. Missing values were imputed using the minimum NSAF determined across the samples. Finally, for each protein the KO/WT ratio was determined by dividing the average of the three NO NSAF values by the average of the three WT NSAF values. *P* values were determined using a two-sided *t* test.

ELISA

Sera from blood was collected via saphenous vein from 6–10-month-old mice while fecal samples were weighed and resuspended at a ratio of 100 mg feces per mL of PBS/0.01% sodium azide/1% (v/v) 100× protease inhibitor cocktail (Sigma). Ninety-six well EIA/RIA plates (Corning) were coated overnight at 4 °C with anti-IgA antibodies (BD Pharmingen) in carbonate buffer, pH 9.6. Washing was done with PBS/T (0.01% Tween-20), blocking was done with PBS/1% BSA and serum and antibodies were diluted in PBS/1% BSA. Serum dilutions were incubated in the coated wells for 2 h, and bound antibodies were detected using corresponding biotinylated rat anti-mouse IgM, IgG1, IgG2b, IgG3 or IgA (BD Pharmingen) for 1 h at RT. This was followed by incubation with HRP-conjugated streptavidin for 1 h and subsequently developed using 2,2-azino-bis (3-ethylbenzothiazoline-6-sulfonic acid) substrate (Sigma). Absorbance was measured at 405 nm in a BioTek Synergy HTX multi-mode reader. Standard curves and relative serum antibody concentrations were calculated using GraphPad Prism v9 software.

Plasmids/construct

pDEST-FLAG, pDEST-EGFP, pDEST-mCherry and pDEST-BirA plasmids were a kind from Dr Anne Claude Gringas. All fusion tags used are located at the N-terminal of the protein of interest. Plasmids containing cDNA of Gng2 and Otub1 were a gift from Dr Sidong Huang. The entry clones for GNG2 and OTUB1 were generated by BP clonase-mediated recombination reactions between vector pDONR221 and purified PCR products containing the full length cDNAs. The primers used for the BP reactions are listed in [Table S6 \(Supplementary material\)](#). Where appropriate, a stop codon was introduced into the C-term ends of the construct. BP- and LR- recombination reactions were performed with BP Clonase II and LR

Clonase II Enzyme mix respectively (Invitrogen). Reactions were stopped by addition of Proteinase K and incubation at 37°C for 10 min. Plasmids were subsequently transformed into either XL10-Gold ultracompetent bacteria or NEB Stable Competent *Escherichia coli*.

Cell lines

HEK293T cells were a gift from Dr Jerry Pelletier (McGill University, Canada) and were cultured in DMEM (Wisent, 319-005-CL) supplemented with 10% fetal bovine serum (FBS) and 1× penicillin-streptomycin (P/S) (Wisent bioproducts, 450-201-EL). The Raji cell line was obtained from ATCC, cultured in RPMI (350-000-CL) supplemented with 20% FBS and 1× P/S. The 2PK-3 cell line were a gift from Dr Michael Gold (University of British Columbia) and were cultured in RPMI 1640 supplemented with 10% heat-inactivated FCS, 50 μM 2-ME, 2 mM glutamine, and 1 mM pyruvate. Stably expressing BirA-Gng2 cell lines were generated in Flp-In T-Rex 293 cells. (Invitrogen; used for BioID and affinity purification coupled to MS analysis). Cells were grown at 37°C in DMEM supplemented with 10% fetal bovine serum and penicillin/streptomycin. Cell lines are routinely tested for mycoplasma using a mycoplasma PCR detection kit (ABM, G238).

Coimmunoprecipitation

HEK293T cells were transfected with indicated plasmids at 60% confluency for 48 h. Cells were washed twice with PBS and collected by cell scraping on ice, in 350 μL high-salt lysis buffer (50 mM Tris, 300 mM NaCl, 1 mM EDTA, 1% Triton X-100). Cell lysates were placed on a rotator for 30 min at 4°C to ensure sufficient lysis, followed by a 15 min incubation at 30°C in 0.25 M CaCl₂ and 250 U benzonase to dissociate DNA-protein interaction. Cell lysates were cleared by centrifugation at maximum speed for 15 min at 4°C. Supernatant was diluted 1:2 with dilution buffer, then placed on 40 μL washed anti-M2 affinity magnetic beads/resin and placed on a rotator overnight at 4°C. Beads/resin were washed twice with low salt wash buffer (50 mM Tris, pH 7.6, 150 mM NaCl, 1 mM EDTA) and twice with TBS (20 mM Tris, 150 mM NaCl) buffer. Proteins were eluted in 1× FLAG peptides (Sigma). Protein was subjected to immunoblotting as above.

GNG2 stability analysis

Naïve splenic B cells were purified from either control or B-Otub1-fl/fl mice, activated with 20 μg/mL LPS, and electroporated 24 h later. Control or B-Otub1-fl/fl were washed with PBS and resuspended in electroporation buffer (9 mM NaPO₄ pH 7.2; KCl 500 μM; MgCl₂ 1 mM; 2 mM HEPES; Sodium Succinate 2.4 mM in endotoxin free water). Primary B cells were electroporated with 200 ng of EGFP-Gng2 using the 4D-Nucleofector System (Lonza). Cells were subsequently resuspended in complete RPMI media at 1 × 10⁶/mL and grown until indicated times. WT and Otub1 depleted Raji-Cas9 cells were washed with PBS and resuspended in electroporation buffer (5 mM KCl; 15 mM MgCl₂; 15 mM HEPES; 150 mM,

Na₂HPO₄/NaH₂PO₄; 50 mM mannitol). Cells were electroporated with 2.5 μg of EGFP-GNG2 or mCherry plasmid using the 4D-Nucleofector System (Lonza). Cells were subsequently resuspended in complete RPMI media at 1 × 10⁵/mL and grown until indicated times. The percentage of GFP or mCherry positive cells were determined using LSRFortessa (BD). For cycloheximide chase experiments, 48 h after transfection, cells were incubated with 100 μg/mL cycloheximide (Sigma) for the indicated time periods.

CRISPR model generation

To generate CRISPR knockout cells, single guide RNAs were cloned into lentiGuide-puro vector (Addgene#: 52963), lentiCRISPRv2 vector (Addgene#: 52961) or MSCV-Cas9-2A-GFP-sgRNA (Addgene#: 124889). The sequence of sgRNAs used in this study are listed in Table S6 (Supplementary material). Lentiviral transduction of cells for sgRNA experiments was performed as previously described.⁶³ Briefly, HEK293T cells were transfected with lentiGuide-puro or lentiCRISPRv2 constructs together with psPAX.2 and VSV-g third generation lentiviral packaging system using the calcium phosphate transfection method. Viral supernatants were collected 48, 60, 72, and 96 h posttransfection and concentrated using PEG6000 (Sigma). For Raji-Cas9 cells, 200,000 cells in 2 mL of media were spinfected with concentrated virus and 8 μg/mL For HEK293T cells, concentrated virus and 8 μg/mL of polybrene was added to 200,000 cells and incubated for 6 h, before media was removed and replaced with regular culture media. Two days posttransduction, the cells were selected with 2 μg/mL puromycin for 3 days. For Raji-Cas9 cells, 200,000 cells in 2 mL of media were spinfected with concentrated virus and 8 μg/mL of polybrene at 1000 g for 60 min. The lentivirus containing medium was removed immediately after spinfection and replaced with regular culture media. Individual cell sorting was conducted into 96 well plates using a FACSAria II (BD Biosciences) to establish single cell colonies. Retroviral particles were also generated by using calcium phosphate transfection into HEK293T as above but using pCL-Eco (Addgene #12371) packaging plasmid instead. Approximately 1 × 10⁵ 2PK-3 cells were placed in a 24-well plate along with the retroviral supernatant and the cells were centrifuged at 1340 g (2400 r.p.m.) for 2 h at room temperature. The viral supernatant was aspirated and subsequently resuspended in growth medium. Twenty-four hours after, cells were again spinfected with fresh retrovirus for a second time. Forty-eight hours after the second spinfection, the highest 10% of GFP-expressing cells were single cell sorted into 96 well plates using aFACSAria II (BD Biosciences).

BioID sample preparation for mass spectrometry

Samples were processed from Flp-In T-Rex 293 cells stably expressing FLAG-BirA-Gng2 as previously described.⁶³ Briefly, at 70% confluency, induction of fusion protein expression was achieved by adding 1 μM tetracycline to the cells for 24 h. After induction, the media was supplemented with 50 μM biotin, for an additional 24 h. Cells were then

harvested and washed twice with PBS. Pellets were subsequently resuspended in cold RIPA buffer containing: 50 mM Tris-HCl pH 7.4, 150 mM NaCl, 1 mM EDTA, 1% NP-40, 0.1% SDS, 0.5% sodium deoxycholate, 1 mM PMSF, 1 mM dithiothreitol, 1:500 Sigma-Aldrich protease inhibitor cocktail (P8340, Sigma). Cell homogenates were sonicated and 250 U benzonase was added before high-speed centrifugation (12,000 rpm, 30 min). Supernatants were incubated with pre-washed streptavidin-sepharose beads (GE, #17-5113-01) at 4 °C with rotation for 3 h. Beads were collected by centrifugation (2,000 rpm 1 min), washed twice with RIPA buffer and three times with 50 mM ammonium bicarbonate (ABC, pH 8.2). Beads were resuspended in 50 mM ABC and on-bead digestion was achieved by adding 1 µg trypsin (Sigma-Aldrich T6567) to the suspension for overnight incubation at 37 °C with rotation. Supernatant containing peptides was collected by centrifugation and pooled with supernatants from two following washes with HPLC-grade H₂O. Digestion was ended with the addition of formic acid to a final concentration of 5%. Samples were centrifuged (12,000 rpm for 10 min), and the supernatants were dried in a SpeedVac for 3 h at high rate. Peptides were resuspended in 5% formic acid and kept at -80 °C for mass spectrometric analysis. MS processing and protein analysis were carried out as previously described.⁶³ All proteomic data have been deposited in the MassIVE depository database (MSV000091229).

BioID functional enrichment analysis

The g:Profiler tool was used to identify functional enrichment analysis (Benjamini-Hochberg FDR < 0.05). Overrepresentation analyses of GO terms, KEGG pathways and CORUM complexes were executed with the R package gprofiler2⁶⁴ by excluding electronic annotations and statistically correcting *P* values with the false discovery rate (FDR) correction method. We selected statistically significant terms and presented the results in dot plots with the ggplot2 R package.

$$\frac{gMFI(\text{individual time point post CXCL13 activation}) - gMFI(0s \text{ time point})}{gMFI(0s \text{ time point})} \times 100$$

Calcium flux analysis

Splenocytes were isolated into RPMI/10% heat inactivated FCS, incubated for 30 min at 37 °C on 10 cm tissue culture plates to eliminate adherent macrophages. RBCs were lysed using RBC lysis buffer and then washed twice with RPMI/0.5% fatty acid free (FAF) BSA (Sigma). 1×10^7 splenocytes were stained with Indo-1, AM (ThermoFisher) in the presence of 0.02% Pluronic F127 (ThermoFisher) for 30 min at 37 °C/5% CO₂. In the last 10 min, cells were counterstained with B220, CD21 and CD23 to allow for B cell subset discrimination. 2PK-3 cells were also stained with Indo-1, AM in 0.02%

Pluronic F127 for acquisition, however, without the need for RBC lysis or staining with additional antibodies. Cells were washed and prewarmed to 37 °C before analysis. Indo-1 fluorescence emission was measured using a 355 nm UV laser and 379/28 (Indo-1 bound) and 515/30 (Indo-1 free) filter sets on a LSRFortessa (BD) flow cytometer. The ratio was calculated as Indo-1 bound/Indo-1 free.

Phospho-RS6 flow cytometry staining

Murine splenocytes were prepared similar to calcium flux analysis. Cells were stained with B220, CD21 and CD23 for B cell subset discrimination, prewarmed at 37 °C for 30 min, before activation with Cxcl12 (100 ng/mL). At indicated time points, cells were immediately fixed using FoxP3 Transcription Factor Fixation/Permeabilization Concentrate and Diluent (Life Technologies) according to manufacturer's suggestions. Cells were then blocked with 1% rat serum, before staining with pRS6-PE antibody for 30 min.

F-actin polymerization

B cells were mashed through a 70 µm filter into 0.1% FAF-BSA(Sigma)/25 mM HEPES/RPMI. Cells were lysed with RBC lysis buffer, stained with B220, CD21, CD23 and CD24 to allow the B cell subsets to be distinguished. The cells were rested at 3×10^6 cells/mL in 0.1% FAF-BSA/25 mM HEPES/RPMI medium for 30 min prior to the F-actin polymerization assay. Splenic cells were stimulated with CXCL13 (1 µg/mL; Biolegend) for various time points. At each time point (0 s to 300 s), 100 µL was taken from the cell suspension and the cells immediately fixed in 4% paraformaldehyde (Sigma) for 10 min. The cells were then washed twice with 0.1% TritonX-100/RPMI and permeabilized for 4 min in 0.1% TritonX-100/RPMI at RT. Cells were then stained with Alexa Fluor647TM phalloidin for 30 min and washed twice with 0.1% TritonX-100/RPMI before acquiring by flow cytometry. F-actin polymerization percentage was calculated using geometric mean fluorescence intensity (gMFI) as follows:

Transwell migration assay

Splenocytes were prepared as for calcium flux analysis but were additionally rested for at least 1 h at 5% CO₂ at 37 °C post-RBC lysis. Chemotaxis assays were performed using 1×10^6 total cells per 5 µM transwell (Corning Costar Corp., Acton, MA) toward Cxcl12 (Biolegend), Cxcl13 (Biolegend) or S1P (Sigma). Cells that migrated to the lower chamber were stained with B220, CD21 and CD23 antibodies and enumerated by collecting events for 150 s on a LSRFortessa (BD) flow cytometer.

Single-cell RNA-seq library preparation

Control and B-Otub1-fl/fl littermates from two litters were processed by scRNA-seq in two batches (2 mice/genotype total, 1 mouse/genotype in each batch, all males). Mice were sacrificed at 56 days. Spleens were harvested into MACS buffer (0.5% BSA, 2 mM EDTA, PBS) on ice and minced through a 40 μ m strainer. Cells were lysed with 2 mL RBC lysis buffer (Sigma-Aldrich) for 5 min at room temperature. The reaction was quenched with 10 mL MACS buffer and samples were centrifuged at 700 g for 5 min. Cells were resuspended to 10^7 cells/mL in MACS buffer with 10 μ L/ 10^7 cells anti-B220 MACS microbeads (Miltenyi) and rotated for 20 min at 4 °C. Stained cells were passed through LS columns (Miltenyi) and washed three times with 3 mL MACS buffer. Cells were spun down at 700 g for 5 min and resuspended in PBS + 0.04% ultra-pure BSA. Library preparation was performed with the 10X Chromium Single Cell 3' v2 chemistry protocol (10X Genomics) for a target of 10,000 cells/sample.⁶⁵ Libraries were sequenced on the Illumina HiSeq4000 platform.

scRNA-seq data analysis

Reads were trimmed, demultiplexed, aligned to the mm10 genome, and unique transcripts were counted using the 10X Genomics Cell Ranger pipeline (v2.0.2 for batch 1, v2.1.1 for batch 2). Quality control of expression matrices, clustering, and visualization was performed in R (v3.5.0) with methods from the Seurat package (v2.3.4).^{66,67} Genes with expression in <3 cells and cells with <200 detected genes were excluded. Cells with greater than 10,000 UMIs or >12% mitochondrial content were removed. The data was scaled to 10,000 UMIs per cell and log-normalized. Samples were first clustered separately. Briefly, variable genes were defined as genes with average expression between 0.0125 and 3 and with dispersion ≥ 0.5 . Number of UMIs and mitochondrial content were regressed from the normalized gene counts and the residuals were z-scored gene-wise. Dimensionality reduction was applied to the variable genes using principal component analysis (PCA), with 50 PCs computed. The first 20 PCs were used as input for visualization in two dimensions using uniform manifold approximation and projection (UMAP)⁴ and as input for clustering. Cells were clustered using a shared nearest neighbor (SNN) modularity optimization algorithm using the Smart Local Moving algorithm on a k-nearest neighbor graph with $k=30$ and the resolution parameter set to 0.8. The resulting clusters were labeled as B cells or non-B cells based on expression of *Cd19*, *Cd79a*, and *Ms4a1*. Cells expressing *Otub1* in B cell clusters of B-Otub1-fl/fl samples were removed prior to joint analysis of all samples. Joint analysis of all samples was performed as described for samples separately, with counts of each sample combined and treated as one. The first 30 PCs of the 50 computed were used for visualization and clustering. Cell cycle scores for G2/M and S phases were computed as implemented in Seurat,⁶⁷ by calculating the average expression of G2/M and S phase-associated gene lists in each single cell and subtracting the average expression of control gene lists. Cluster markers were computed for each cluster compared to all

other cells using the Wilcoxon rank sum test, requiring that a gene is detected in at least 25% of cells in the cluster or outside the cluster and has an average log₂ fold change of at least 0.25 to be tested. Cell type labels for clusters from the joint analysis were assigned based on cluster markers, as well as expression of canonical cell type-specific markers (B cells: *Cd19*, *Cd79a*, *Ms4a1*; plasma cells: *Mzb1*, *Jchain*, *Xbp1*; NK cells: *Ncr1*, *Nkg7*, *Gzma*; macrophages: *Adgre1*, *C1qa*, *Csf1r*; T cells: *Cd3e*, *Cd8a*, *Skap1*; monocytes: *Cd68*, *Fcer1g*, *Itgax*, *Lyz2*, *Tyrobp*; dendritic cells: *Cd86*, *Clec9a*, *Xcr1*, *Cd207*). Follicular (FoB), marginal zone (MzB), and transitional (TrB) B cell subsets were identified using ssGSEA with code adapted from the GSVA package (v1.27.0)⁶⁸ and signatures from^{46,47}. Differential expression analysis between WT and Otub1-cKO was performed per cluster, with each cluster down sampled to equal cell numbers between conditions. DE genes were obtained using the Wilcoxon rank sum test, requiring that a gene is detected in at least 25% of cells in either condition and has an average log₂ fold change of at least 0.25 to be tested.

Pseudotemporal ordering and trajectory reconstruction

The trajectory of control and B-Otub1-fl/fl B cells was inferred using the R package Monocle2 v.2.8.0.^{69,70,71} Only B cell clusters were included in the analysis (Fig. 4A). Dimensionality reduction was performed using the discriminative dimensionality reduction with trees algorithm,⁶⁹ with the effect of the number of genes expressed and the mitochondrial percentage removed. The most variant genes were used to order cells along the tree. Cells were assigned a pseudotime according to their distance from the root state, which was manually selected. To display the relationship between cells in pseudotime, a minimum spanning tree was generated.

Immunostaining

Immunohistochemistry was performed using a protocol adapted from an earlier study.⁷² Briefly, spleens and LNs were fixed in PLP buffer (0.05 M phosphate buffer, 0.1 M l-lysine, 2 mg/mL NaIO₄, and 10 mg/mL paraformaldehyde, pH 7.4) overnight followed by cryoprotection in 30% sucrose overnight. Tissue was frozen in Tissue-Tek OCT compound and stored at -80 °C until sectioning. Spleens and LN were cut at -20 °C into 20 μ m thick sections using a Leica CM3050S cryostat. Sections were blocked in buffer (0.1 M Tris, 1% FBS, 0.3% Triton X-100, 1% gelatin from cold water fish scales) and stained with a primary antibody against MOMA-1 (Abcam) overnight followed by a goat anti-rabbit AF594 (Invitrogen) secondary antibody. Spleen sections were incubated with 1% normal rat serum for 1 h and subsequently stained with conjugated antibody using IgD-FITC (BD) and IgM-AF647 (BD) overnight. LN sections were stained with CD3 primary antibody, followed by goat anti-rat AF555 (Invitrogen), and lastly IgM-BV421 (Biolegend), IgD-FITC (BD) and CD169-AF647 (Biolegend) overnight. Stained sections were fixed on slides using Fluoromount-G for imaging and kept at 4 °C until image capture.

Imaging and analysis

Confocal microscopy images were taken with Zeiss LSM 880. Images shown were taken with Plan-Apochromat objective 20× (N.A = 0.8) and stitched together with ZEN software. 2D image projections were generated and processed using Fiji (ImageJ). Z-slices were summed, and MZB and FoB ROIs defined by the MOMA-1 boundary. Mean fluorescence intensity was quantified for IgM and IgD within each ROI.

Adoptive transfer of FoB cells

Spleens from CD45.2 congenic donor mice (control or B-Otub1-fl/fl) were collected and mechanically dissociated. Red blood cells were lysed using red blood cell lysing buffer (Sigma). FoB cells were sorted from splenic B cells as B220⁺CD21⁺CD23⁺ on an FACSria II (BD Biosciences). Cells were resuspended in PBS on ice and 2 million cells were injected i.v. in 200 μL into CD45.1 congenic recipient mice. Cells from the spleen were analyzed 28 days after transfer for CD45.1 and CD45.2 expression and B220⁺CD21⁺CD23⁺ to distinguish FoB from MZB cells.

Statistical analyses

All quantitative experiments are plotted with mean ± S.E.M (unless otherwise stated) with the number of independent experiments performed stated in the figure legends. Statistical significance was determined using the tests indicated in the legend. A *P* value < 0.05 was considered significant. All statistical analyses were performed in Prism v9 (GraphPad).

Acknowledgments

We are grateful to Dr D. Durocher, Dr S. Richard, Dr M. Reth, Dr F.E. Mercier, and Dr A.C. Gringas for plasmids and other reagents. We are grateful to Dr F.E. Mercier for CD45.1^{STEM} mice. We thank Dr. KK Mann, A. Xue, D. Grapton, and Dr. E. Pinedo-Carpio for technical help. We thank The Center for Phenogenomics (TCP, Toronto) for the generation of the different Otub1 strains. We thank the staff of the animal facility and the flow cytometry core facility (both at Lady Davis Institute for Medical Research). We also thank L. Taylor at the proteomics platform at the RIMUHC and D. Foubert at the mass spectrometry and proteomics platform at the IRCM. Data analysis were enabled by computer and storage resources provided by Compute Canada and Calcul Québec. V.M.L. is funded by the Cole Foundation Fellowship and a Fonds de recherche Santé Quebec (FRSQ) Doctoral award. C.S. is funded by a Canadian Institutes of Health Research Doctoral Award. A.B. is funded by a CIHR Canada Graduate Scholarship and a FRSQ Masters Training Scholarship. E.S.C. is funded by a FRQS Postdoctoral Training Scholarship. S.F. is funded by the Cole Foundation Fellowship. C.L.K. is supported by a salary award from the FRQS. J.N.M. is a Canada Research Chair for Immune Cell Dynamics. A.O. is a Canada Research Chair in Genome Stability and Haematological Malignancies. C.H.B. is grateful to Genome Canada for financial support through the Genomics Technology Platform (GTP) (264PRO). C.H.B. is also grateful for support from the Segal McGill Chair in Molecular Oncology at McGill University (Montreal, Quebec, Canada), and for support from the Warren Y. Soper Charitable Trust and the Alvin Segal Family Foundation to the Jewish General Hospital (Montreal, Quebec, Canada). This research was supported by two CIHR Project Grants (PJT-361708, PJT-156086), a Transition Grant from the Cole

Foundation and an internal Operating Fund from the Sir Mortimer B. Davis Foundation of the Jewish General Hospital.

Author Contributions

A.O. and J.N.M. conceived the project, designed the research, and obtained funding for this study. V.M.L. performed most of the experiments, analyzed most of data, except the scRNA-seq and the confocal microscopy images, and wrote the manuscript with A.O. and J.N.M. C.S. and A.B. performed the tissue sectioning and immunohistochemistry experiments, analyzed, and quantified the confocal images with input from J.N.M. S.W. analyzed the scRNA-seq data and generated the associated figures under the supervision of C.K. S.F. optimized and performed the co-IP experiments. W.L.P. performed the ELISA experiments and analyzed the data with the help of T.Z. Z.A. conducted the actin polymerization assay with V.M.L. Z.S.B. advised on the mouse work and associated experimental design. R.P.Z. analyzed the proteomics data completed in splenic B cells under the supervision of C.H.B. J.B. analyzed the GNG2 BioID and generated the associated figures with input from J.F.C. All authors provided input during the writing of the manuscript.

Disclosure Statement

C.H.B. is the C.S.O. of MRM Proteomics, Inc. and the C.T.O. of Molecular You. R.P.Z. is the CEO of MRM Proteomics, Inc. The other authors declare no conflict of interest.

ORCID

Alexandre Orthwein  <http://orcid.org/0000-0002-7350-3413>

Data Availability Statement

The data that support the findings of this study are openly available in the MassIVE depository database (<https://massive.ucsd.edu/ProteoSAFe/static/massive.jsp>), reference MSV000091229.

References

- Zinngrebe J, Montinaro A, Peltzer N, Walczak H. Ubiquitin in the immune system. *EMBO Rep.* 2014;15:28–45. doi:10.1002/embr.201338025.
- Komander D, Rape M. The ubiquitin code. *Annu Rev Biochem.* 2012;81:203–229. doi:10.1146/annurev-biochem-060310-170328.
- Harrigan JA, Jacq X, Martin NM, Jackson SP. Deubiquitylating enzymes and drug discovery: emerging opportunities. *Nat Rev Drug Discov.* 2018;17:57–78. doi:10.1038/nrd.2017.152.
- Clague MJ, Heride C, Urbé S. The demographics of the ubiquitin system. *Trends Cell Biol.* 2015;25:417–426. doi:10.1016/j.tcb.2015.03.002.
- Edelmann MJ, Iphöfer A, Akutsu M, Altun M, di Gleria K, Kramer HB, Fiebigler E, Dhe-Paganon S, Kessler BM. Structural basis and specificity of human otubain 1-mediated deubiquitination. *Biochem J.* 2009;418:379–390. doi:10.1042/BJ20081318.
- Wang T, Yin L, Cooper EM, Lai MY, Dickey S, Pickart CM, Fushman D, Wilkinson KD, Cohen RE, Wolberger C. Evidence for bidentate substrate binding as the basis for the K48 linkage specificity of otubain 1. *J Mol Biol.* 2009;386:1011–1023. doi:10.1016/j.jmb.2008.12.085.
- Chau V, Tobias JW, Bachmair A, Marriott D, Ecker DJ, Gonda DK, Varshavsky A. A multiubiquitin chain is confined to specific lysine in a targeted short-lived protein. *Science.* 1989;243:1576–1583. doi:10.1126/science.2538923.
- Finley D, Sadis S, Monia BP, Boucher P, Ecker DJ, Crooke ST, Chau V. Inhibition of proteolysis and cell cycle progression in a

- multiubiquitination-deficient yeast mutant. *Mol Cell Biol.* 1994;14:5501–5509. doi:10.1128/mcb.14.8.5501-5509.1994.
9. Soares L, Seroogy C, Skrenta H, Anandasabapathy N, Lovelace P, Chung CD, Engleman E, Fathman CG. Two isoforms of otubain 1 regulate T cell anergy via GRAIL. *Nat Immunol.* 2004;5:45–54. doi:10.1038/ni1017.
 10. Herhaus L, Al-Salihi M, Macartney T, Weidlich S, Sapkota GP. OTUB1 enhances TGFbeta signalling by inhibiting the ubiquitylation and degradation of active SMAD2/3. *Nat Commun.* 2013;4:2519. doi:10.1038/ncomms3519.
 11. Li Y, Yang JY, Xie X, Jie Z, Zhang L, Shi J, Lin D, Gu M, Zhou X, Li HS, et al. Preventing abnormal NF-kappaB activation and autoimmunity by Otub1-mediated p100 stabilization. *Cell Res.* 2019;29:474–485. doi:10.1038/s41422-019-0174-3.
 12. Nakada S, Tai I, Panier S, Al-Hakim A, Iemura S, Juang YC, O'Donnell L, Kumakubo A, Munro M, Sicheri F, et al. Non-canonical inhibition of DNA damage-dependent ubiquitination by OTUB1. *Nature.* 2010;466:941–946. doi:10.1038/nature09297.
 13. Juang YC, Landry MC, Sanches M, Vittal V, Leung CC, Ceccarelli DF, Mateo AR, Pruneda JN, Mao DY, Szilard RK, et al. OTUB1 co-opts Lys48-linked ubiquitin recognition to suppress E2 enzyme function. *Mol Cell.* 2012;45:384–397. doi:10.1016/j.molcel.2012.01.011.
 14. Tamayo E, Alvarez P, Merino R. TGFbeta superfamily members as regulators of B cell development and function-implications for autoimmunity. *Int J Mol Sci.* 2018;19:3928. doi:10.3390/ijms19123928.
 15. Sasaki Y, Iwai K. Roles of the NF-kappaB pathway in B-lymphocyte biology. *Curr Top Microbiol Immunol.* 2016;393:177–209. doi:10.1007/82_2015_479.
 16. Gullickson P, Xu YW, Niedernhofer LJ, Thompson EL, Yousefzadeh MJ. The role of DNA repair in immunological diversity: from molecular mechanisms to clinical ramifications. *Front Immunol.* 2022;13:834889. doi:10.3389/fimmu.2022.834889.
 17. LeBien TW, Tedder TF. B lymphocytes: how they develop and function. *Blood.* 2008;112:1570–1580. doi:10.1182/blood-2008-02-078071.
 18. Pillai S, Cariappa A. The follicular versus marginal zone B lymphocyte cell fate decision. *Nat Rev Immunol.* 2009;9:767–777. doi:10.1038/nri2656.
 19. Cyster JG, Allen CDC. B cell responses: cell interaction dynamics and decisions. *Cell.* 2019;177:524–540. doi:10.1016/j.cell.2019.03.016.
 20. Mebius RE, Kraal G. Structure and function of the spleen. *Nat Rev Immunol.* 2005;5:606–616. doi:10.1038/nri1669.
 21. Luo Y, Zhang X, Chen R, Li R, Liu Y, Zhang J, Liu Q, Si M, Liu J, Wu B, et al. USP10 regulates B cell response to SARS-CoV-2 or HIV-1 nanoparticle vaccines through deubiquitinating AID. *Signal Transduct Target Ther.* 2022;7:7. doi:10.1038/s41392-021-00858-z.
 22. Satpathy S, Wagner SA, Beli P, Gupta R, Kristiansen TA, Malinova D, Francavilla C, Tolar P, Bishop GA, Hostager BS, et al. Systems-wide analysis of BCR signalosomes and downstream phosphorylation and ubiquitylation. *Mol Syst Biol.* 2015;11:810. doi:10.15252/msb.20145880.
 23. Li X, Gadzinsky A, Gong L, Tong H, Calderon V, Li Y, Kitamura D, Klein U, Langdon WY, Hou F, et al. Cbl ubiquitin ligases control B cell exit from the germinal-center reaction. *Immunity.* 2018;48:530–541 e6. doi:10.1016/j.immuni.2018.03.006.
 24. Pereira JP, Kelly LM, Cyster JG. Finding the right niche: B-cell migration in the early phases of T-dependent antibody responses. *Int Immunol.* 2010;22:413–419. doi:10.1093/intimm/dxq047.
 25. Pasupala N, Morrow ME, Que LT, Malynn BA, Ma A, Wolberger C. OTUB1 non-catalytically stabilizes the E2 ubiquitin-conjugating enzyme UBE2E1 by preventing its autoubiquitination. *J Biol Chem.* 2018;293:18285–18295. doi:10.1074/jbc.RA118.004677.
 26. Hobeika E, Thiemann S, Storch B, Jumaa H, Nielsen PJ, Pelanda R, Reth M. Testing gene function early in the B cell lineage in mb1-cre mice. *Proc Natl Acad Sci USA.* 2006;103:13789–13794. doi:10.1073/pnas.0605944103.
 27. Hardy RR, Carmack CE, Shinton SA, Kemp JD, Hayakawa K. Resolution and characterization of pro-B and pre-pro-B cell stages in normal mouse bone marrow. *J Exp Med.* 1991;173:1213–1225. doi:10.1084/jem.173.5.1213.
 28. Saldana M, VanderVorst K, Berg AL, Lee H, Carraway KL. Otubain 1: a non-canonical deubiquitinase with an emerging role in cancer. *Endocr Relat Cancer.* 2019;26:R1–R14. doi:10.1530/ERC-18-0264.
 29. Iglesias-Gato D, Chuan YC, Jiang N, Svensson C, Bao J, Paul I, Egevad L, Kessler BM, Wikstrom P, Niu Y, et al. OTUB1 deubiquitinating enzyme promotes prostate cancer cell invasion in vitro and tumorigenesis in vivo. *Mol Cancer.* 2015;14:8. doi:10.1186/s12943-014-0280-2.
 30. Khan SM, Sung JY, Hébert TE. Gbetagamma subunits—different spaces, different faces. *Pharmacol Res.* 2016;111:434–441. doi:10.1016/j.phrs.2016.06.026.
 31. Khan SM, Sleno R, Gora S, Zylbergold P, Laverdure J-P, Labbé J-C, Miller GJ, Hébert TE. The expanding roles of Gbetagamma subunits in G protein-coupled receptor signaling and drug action. *Pharmacol Rev.* 2013;65:545–577. doi:10.1124/pr.111.005603.
 32. Gurevich VV, Gurevich EV. GPCR signaling regulation: the role of GRKs and arrestins. *Front Pharmacol.* 2019;10:125. doi:10.3389/fphar.2019.00125.
 33. Feng Y, Su Y, Ma C, Jing Z, Yang X, Zhang D, Xie M, Li W, Wei J. 3'UTR variants of TNS3, PHLDDB1, NTN4, and GNG2 genes are associated with IgA nephropathy risk in Chinese Han population. *Int Immunopharmacol.* 2019;71:295–300. doi:10.1016/j.intimp.2019.03.041.
 34. Yoshida H, Lareau CA, Ramirez RN, Rose SA, Maier B, Wroblewska A, Desland F, Chudnovskiy A, Mortha A, Dominguez C, et al. The cis-regulatory atlas of the mouse immune system. *Cell.* 2019;176:897–912.e20. doi:10.1016/j.cell.2018.12.036.
 35. Roux KJ, Kim DI, Burke B. BioID: a screen for protein-protein interactions. *Curr Protoc Protein Sci.* 2013;74:19.23.1–19.23.14. doi:10.1002/0471140864.ps1923s74.
 36. Legler DF, Thelen M. New insights in chemokine signaling. *F1000Res.* 2018;7:95. doi:10.12688/f1000research.13130.1.
 37. Nie Y, Waite J, Brewer F, Sunshine MJ, Littman DR, Zou YR. The role of CXCR4 in maintaining peripheral B cell compartments and humoral immunity. *J Exp Med.* 2004;200:1145–1156. doi:10.1084/jem.20041185.
 38. Förster R, Mattis AE, Kremmer E, Wolf E, Brem G, Lipp M. A putative chemokine receptor, BLR1, directs B cell migration to defined lymphoid organs and specific anatomic compartments of the spleen. *Cell.* 1996;87:1037–1047. doi:10.1016/s0092-8674(00)81798-5.
 39. Cinamon G, Matloubian M, Lesneski MJ, Xu Y, Low C, Lu T, Proia RL, Cyster JG. Sphingosine 1-phosphate receptor 1 promotes B cell localization in the splenic marginal zone. *Nat Immunol.* 2004;5:713–720. doi:10.1038/ni1083.
 40. Clapham DE. Calcium signaling. *Cell.* 2007;131:1047–1058. doi:10.1016/j.cell.2007.11.028.
 41. Kennedy BK, Lamming DW. The mechanistic target of rapamycin: the grand conductor of metabolism and aging. *Cell Metab.* 2016;23:990–1003. doi:10.1016/j.cmet.2016.05.009.
 42. Robles-Molina E, Dionisio-Vicuña M, Guzmán-Hernández ML, Reyes-Cruz G, Vázquez-Prado J. Gbetagamma interacts with mTOR and promotes its activation. *Biochem Biophys Res Commun.* 2014;444:218–223. doi:10.1016/j.bbrc.2014.01.044.
 43. Wang F. The signaling mechanisms underlying cell polarity and chemotaxis. *Cold Spring Harb Perspect Biol.* 2009;1:a002980. doi:10.1101/cshperspect.a002980.
 44. Moratz C, Kehrl JH. In vitro and in vivo assays of B-lymphocyte migration. *Methods Mol Biol.* 2004;271:161–171. doi:10.1385/1-59259-796-3:161.
 45. Ho MK, Su Y, Yeung WW, Wong YH. Regulation of transcription factors by heterotrimeric G proteins. *Curr Mol Pharmacol.* 2009;2:19–31. doi:10.2174/187446721090210019.
 46. Kin NW, Crawford DM, Liu J, Behrens TW, Kearney JF. DNA microarray gene expression profile of marginal zone versus follicular B cells and idiotype positive marginal zone B cells before and after immunization with *Streptococcus pneumoniae*. *J Immunol.* 2008;180:6663–6674. doi:10.4049/jimmunol.180.10.6663.
 47. Kleiman E, Salyakina D, De Heusch M, Hoek KL, Llanes JM, Castro I, Wright JA, Clark ES, Dykxhoorn DM, Capobianco E, et al. Distinct transcriptomic features are associated with transitional and mature

- B-cell populations in the mouse spleen. *Front Immunol.* 2015;6:30. doi:10.3389/fimmu.2015.00030.
48. Radice E, Ameti R, Melgrati S, Foglierini M, Antonello P, Stahl RAK, Thelen S, Jarrossay D, Thelen M. Marginal zone formation requires ACKR3 expression on B cells. *Cell Rep.* 2020;32:107951. doi:10.1016/j.celrep.2020.107951.
 49. Schmidt TH, Bannard O, Gray EE, Cyster JG. CXCR4 promotes B cell egress from Peyer's patches. *J Exp Med.* 2013;210:1099–1107. doi:10.1084/jem.20122574.
 50. Okada T, Ngo VN, Ekland EH, Förster R, Lipp M, Littman DR, Cyster JG. Chemokine requirements for B cell entry to lymph nodes and Peyer's patches. *J Exp Med.* 2002;196:65–75. doi:10.1084/jem.2002201.
 51. Torres M. Chapter two—Heterotrimeric G protein ubiquitination as a regulator of G protein signaling. *Prog Mol Biol Transl Sci.* 2016;141:57–83. doi:10.1016/bs.pmbts.2016.03.001.
 52. Hicke L, Riezman H. Ubiquitination of a yeast plasma membrane receptor signals its ligand-stimulated endocytosis. *Cell.* 1996;84:277–287. doi:10.1016/s0092-8674(00)80982-4.
 53. Zhu M, Torres MP, Kelley JB, Dohlman HG, Wang Y. Pheromone- and RSP5-dependent ubiquitination of the G protein beta subunit Ste4 in yeast. *J Biol Chem.* 2011;286:27147–27155. doi:10.1074/jbc.M111.254193.
 54. Hamilton MH, Cook LA, McRackan TR, Schey KL, Hildebrandt JD. Gamma 2 subunit of G protein heterotrimer is an N-end rule ubiquitylation substrate. *Proc Natl Acad Sci USA.* 2003;100:5081–5086. doi:10.1073/pnas.0831228100.
 55. Obin M, Lee BY, Meinke G, Bohm A, Lee RH, Gaudet R, Hopp JA, Arshavsky VY, Willardson BM, Taylor A. Ubiquitylation of the transducin betagamma subunit complex. Regulation by phosducin. *J Biol Chem.* 2002;277:44566–44575. doi:10.1074/jbc.M205308200.
 56. Dalwadi H, Wei B, Schrage M, Spicher K, Su TT, Birnbaumer L, Rawlings DJ, Braun J. B cell developmental requirement for the G alpha i2 gene. *J Immunol.* 2003;170:1707–1715. doi:10.4049/jimmunol.170.4.1707.
 57. Hwang IY, Park C, Luong T, Harrison KA, Birnbaumer L, Kehrl JH. The loss of Gnai2 and Gnai3 in B cells eliminates B lymphocyte compartments and leads to a hyper-IgM like syndrome. *PLoS One.* 2013;8:e72596. doi:10.1371/journal.pone.0072596.
 58. Bowman EP, Campbell JJ, Soler D, Dong Z, Manlongat N, Picarella D, Hardy RR, Butcher EC. Developmental switches in chemokine response profiles during B cell differentiation and maturation. *J Exp Med.* 2000;191:1303–1318. doi:10.1084/jem.191.8.1303.
 59. Allende ML, Tuymetova G, Lee BG, Bonifacino E, Wu YP, Proia RL. S1P1 receptor directs the release of immature B cells from bone marrow into blood. *J Exp Med.* 2010;207:1113–1124. doi:10.1084/jem.20092210.
 60. Han SB, Moratz C, Huang NN, Kelsall B, Cho H, Shi CS, Schwartz O, Kehrl JH. Rgs1 and Gnai2 regulate the entrance of B lymphocytes into lymph nodes and B cell motility within lymph node follicles. *Immunity.* 2005;22:343–354. doi:10.1016/j.immuni.2005.01.017.
 61. Coleman JL, Brennan K, Ngo T, Balaji P, Graham RM, Smith NJ. Rapid knockout and reporter mouse line generation and breeding colony establishment using EUCOMM conditional-ready embryonic stem cells: a case study. *Front Endocrinol (Lausanne).* 2015;6:105. doi:10.3389/fendo.2015.00105.
 62. Mercier FE, Sykes DB, Scadden DT. Single targeted exon mutation creates a true congenic mouse for competitive hematopoietic stem cell transplantation: the C57BL/6-CD45.1(STEM) mouse. *Stem Cell Rep.* 2016;6:985–992. doi:10.1016/j.stemcr.2016.04.010.
 63. Findlay S, Heath J, Luo VM, Malina A, Morin T, Coulombe Y, Djerir B, Li Z, Samiei A, Simo-Cheyoy E, et al. SHLD2/FAM35A co-operates with REV7 to coordinate DNA double-strand break repair pathway choice. *EMBO J.* 2018;37:e100158. doi:10.15252/embj.2018100158.
 64. Raudvere U, Kolberg L, Kuzmin I, Arak T, Adler P, Peterson H, Vilo J. g:Profiler: a web server for functional enrichment analysis and conversions of gene lists (2019 update). *Nucleic Acids Res.* 2019;47:W191–W198. doi:10.1093/nar/gkz369.
 65. Zhang S, Bian Y, Chen A, Zheng H, Gao Y, Hou Y, Li C. Massively parallel sequencing of 231 autosomal SNPs with a custom panel: a SNP typing assay developed for human identification with ion torrent PGM. *Forensic Sci Res.* 2017;2:26–33. doi:10.1080/20961790.2017.1281011.
 66. Stuart T, Butler A, Hoffman P, Hafemeister C, Papalexi E, Mauck WM, 3rd, Hao Y, Stoeckius M, Smibert P, Satija R. Comprehensive integration of single-cell data. *Cell.* 2019;177:1888–1902.e21. doi:10.1016/j.cell.2019.05.031.
 67. Butler A, Hoffman P, Smibert P, Papalexi E, Satija R. Integrating single-cell transcriptomic data across different conditions, technologies, and species. *Nat Biotechnol.* 2018;36:411–420. doi:10.1038/nbt.4096.
 68. Hänzelmann S, Castelo R, Guinney J. GSEA: gene set variation analysis for microarray and RNA-seq data. *BMC Bioinformatics.* 2013;14:7. doi:10.1186/1471-2105-14-7.
 69. Qiu X, Hill A, Packer J, Lin D, Ma YA, Trapnell C. Single-cell mRNA quantification and differential analysis with Census. *Nat Methods.* 2017;14:309–315. doi:10.1038/nmeth.4150.
 70. Qiu X, Mao Q, Tang Y, Wang L, Chawla R, Pliner HA, Trapnell C. Reversed graph embedding resolves complex single-cell trajectories. *Nat Methods.* 2017;14:979–982. doi:10.1038/nmeth.4402.
 71. Trapnell C, Cacchiarelli D, Grimsby J, Pokharel P, Li S, Morse M, Lennon NJ, Livak KJ, Mikkelsen TS, Rinn JL. The dynamics and regulators of cell fate decisions are revealed by pseudotemporal ordering of single cells. *Nat Biotechnol.* 2014;32:381–386. doi:10.1038/nbt.2859.
 72. Bajénoff M, Granjeaud S, Guerder S. The strategy of T cell antigen-presenting cell encounter in antigen-draining lymph nodes revealed by imaging of initial T cell activation. *J Exp Med.* 2003;198:715–724. doi:10.1084/jem.20030167.